J. Fluid Mech. (2025), *vol.* 1007, A12, doi:10.1017/jfm.2025.18

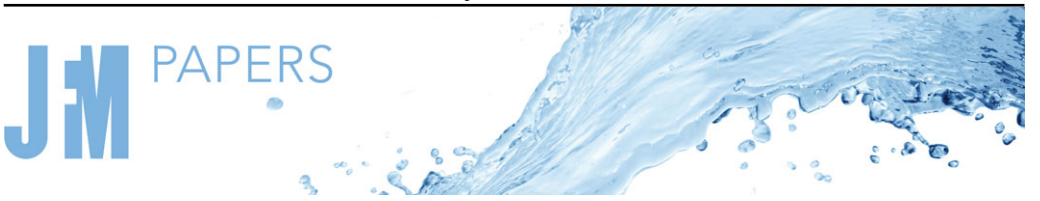

Morphological evolutions and transverse dynamics of strong transverse wave structure in detonations near critical propagation state

Daoping Zhang[1], **Gang Dong**[1] **and Baoming Li**[1]

[1]National Key Laboratory of Transient Physics, Nanjing University of Science and Technology, Nanjing, Jiangsu 210094, PR China

Corresponding author: Gang Dong, gdong@njust.edu.cn

(Received 25 July 2024; revised 4 November 2024; accepted 30 December 2024)

Two-dimensional gaseous detonations near critical propagation state were studied numerically in a channel with stoichiometric H_2/air and H_2/O_2 mixtures. Detonation waves exhibit a mode-locking effect (MLE) in a single-headed mode regime. Increasing the channel width alters the strength and propagation period of the single transverse wave. This leads to MLE failure and the occurrence of the single-dual-headed critical mode, featuring the emergence of a new transverse wave. For a stoichiometric H_2/air mixture, generation of the new transverse wave is due to interactions between the detonation front and the local explosion wave originating from interactions between the transverse wave and unreacted gas pocket downstream. Whereas, for a stoichiometric H_2/O_2 mixture, a transverse wave interacting with the wall produces Mach reflection bifurcation, causing MLE failure and generation of the new transverse wave. Our results show that all transverse waves manifest as strong transverse wave (STW) structures, with most belonging to the second kind, and an acoustic coupling exists between the typical second kind of STW structure and the acoustic wave in the induction zone behind the Chapman–Jouguet detonation front. A high-pressure region close to the STW structure plays a crucial role in exploring the transverse dynamics of this structure. Shock polars with rational assumptions are adopted to predict flow states in this region. The roles of pivotal factors in influencing the flow states and wave structure are clarified, and characteristic pressure values derived adequately represent the STW structure's transverse dynamic behaviours. Lastly, the relationship between the kinematics and kinds of STW structures is unveiled.

Key words: detonation waves, combustion

1. Introduction

A detonation wave is a kind of supersonic combustion wave in which the reaction zone is closely coupled with the shock wave. In the multi-dimensional case, the detonation wave front features a variety of wrinkles, since there are many transverse wave structures on the front. Due to the existence of transverse waves, the pressure behind the detonation wave is locally higher than that behind the one-dimensional plane detonation wave (Han *et al.* 2019), so that the detonation can produce a more powerful destructive force. In addition, the role of transverse effects or transverse waves in the detonations of unstable mixtures has long been recognized as a critical factor in sustaining detonation propagation, as detonations in the real world are difficult to propagate and may fail when the transverse wave is absent (Radulescu & Lee 2002; Zhang, Liu & Yan 2019*a*). Hence, whether from an engineering or fundamental research perspective, the influence of transverse waves should be considered in the study of the detonation phenomenon.

The observation of characteristics of the transverse wave permeates all modes of detonation propagation, from the multi-headed to the single-headed mode. In multi-headed detonation, a series of fish-scale-shaped cellular patterns associated with transverse waves can be presented on the smoke foil (Strehlow, Maurer & Rajan 1969; Monnier *et al.* 2022). The geometrical characteristics of this cell, for instance, cell length (Zadok *et al.* 2023), cell width (Strehlow *et al.* 1969) and cell regularity (Lu, Kaplan & Oran 2021), had been widely analysed to distinguish the characteristics of detonation with different mixtures and investigate the propagation behaviour of the detonation wave.

Merely observing the cellular structure of the detonation is insufficient for understanding the characteristics of transverse waves. The detailed pattern of the detonation wave structure still cannot be intuitively studied from the cellular structure of detonations. For this reason, information about the flow field using various high-speed photography methods had also been obtained. For instance, Pintgen *et al.* (2003) observed a series of transverse wave structures based on the images obtained by the techniques of planar laser-induced fluorescence and schlieren. However, the patterns observed in the images (Edwards, Parry & Jones 1966; Austin, Pintgen & Shepherd 2005; Boulal *et al.* 2018) can be significantly contaminated in most situations due to multi-dimensional effects, which makes the patterns challenging to analyse. Fortunately, more flow field information and clearer shock wave structures can be obtained through numerical means, as reported in work by Mahmoudi *et al.* (2014), Radulescu (2018) and Xiao *et al.* (2021).

With the specific structure of transverse waves known, many researchers have categorized the transverse waves in detonations. Among them, Fickett & Davis (2000) reported transverse wave structures of two types, referred to as weak and strong transverse wave structures; this classification has been recognized and used by many researchers, as in Sharpe (2001), Pintgen *et al.* (2003) and Lee (2008). In general, the definitions of strong and weak transverse wave structures are different from the strong and weak solutions in the Chapman–Jouguet theory of detonation, in which strong and weak solutions feature subsonic and supersonic flows downstream of the detonation wave, respectively. On the one hand, the weak transverse wave structure manifests itself as a simple single Mach reflection structure. Therefore, one can analyse changes in the flow field through relatively simple shock polar theory. The results obtained from the theory can accurately reflect the changes in the state of the flow field. However, the establishment of the shock polar theory utilized data from the flow field, hence it lacks generality.

On the other hand, the strong transverse wave (STW) structure is characterized by having two triple points, thus exhibiting a double Mach reflection structure. The STW structure is often observed in studies concerning spinning detonation in a circular tube

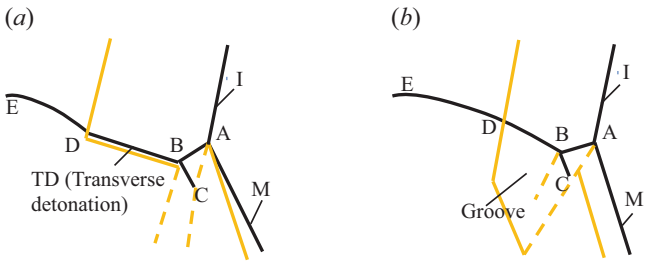

Figure 1. Strong transverse wave structure of (*a*) the first kind and (*b*) the second kind: I – incident front, M – Mach front, A – triple point, B – secondary triple point, C – intersection of transverse wave and slip line, D – intersection of transverse wave and reaction surface and E – rear of transverse wave. Yellow dashed lines and yellow solid lines represent slip lines and reaction surfaces, respectively.

(Tsuboi & Hayashi 2007; Sugiyama & Matsuo 2013). This is due to the presence of a transverse detonation (TD) wave within it, as depicted in figure 1(*a*), which in turn creates a high-energy area. Consequently, this allows researchers to record a luminous helical strip. Since spinning detonations in a circular tube are quasi-steady, Huang, Lefebvre & Van Tiggelen (2000) have combined shock polar theory with experimental measurements to predict the flow field near the TD and compare it with experimental results, a good agreement is obtained. Indeed, Huang *et al.* (2000) heavily rely on experimental data when starting predictions with shock polar theory. From a generalization perspective, it is necessary to develop a method that can independently predict the flow field and identify commonalities of the transverse wave structures. Under the conditions of the highly unstable gas mixtures, the STW structure shown in figure 1(*a*) is more likely to occur, as demonstrated by the results of Yuan *et al.* (2016), Gamezo *et al.* (2000) and Taylor *et al.* (2013). However, due to the complexity of the STW structure, some variations may appear. Sharpe (2001) pointed out that the structure shown in figure 1(*b*) is also one of the STW structures in detonations. The main difference between the two structures is that there is no apparent TD in figure 1(*b*), and a relatively wide "groove" exists between the reaction surfaces behind the Mach front. Clearly, the contributions of the STW in the two figures to the chemical reaction of premixed mixture are quite different. Therefore, this paper refers to the structure shown in figure 1(*a*) as the first kind of STW structure, and defines the structure in figure 1(*b*) as the second kind of STW structure. It is possible for the second kind of STW structure to produce a supersonic flow and the weaker compression behind the transverse wave segment AB.

Early works (Liang & Bauwens 2005*a*,*b*; Austin *et al.* 2005) and recent studies (Rojas Chavez, Chatelain & Lacoste 2023; Cai *et al.* 2023; Watanabe *et al.* 2023) have emphasized the keystone-shaped structures in detonation waves, which are composed of two counter-propagating transverse wave structures. Some unreacted grooves surround these transverse wave structures, consistent with the features of the second kind of STW structure, further highlighting the significance of this kind of structure and the necessity for in-depth research. Unfortunately, quantitative analysis and qualitative understanding of such transverse waves remain scarce.

When detonation propagates close to the critical propagation state, the impact of the transverse wave structure becomes particularly significant. Here, the critical propagation state is defined as the state in which it is difficult for a detonation wave to maintain self-sustained propagation. This propagation state helps us study and understand the characteristics of individual transverse waves, making it highly significant. In the same situation, the mode-locking effect (MLE) of the detonation wave, where the number of

transverse waves does not change with variations in the channel's width, becomes even more pronounced. For example, the MLE allows a single-headed detonation to maintain a single-headed mode within a finite range of channel widths. Taylor *et al.* (2013) have reported on the mode-locking phenomenon of the transverse wave, but the mechanisms behind this phenomenon and its quantitative effects are currently unclear. Meanwhile, the relationship between the MLE, STW dynamics and the reactivity of STW has not been well established. Motivated by the desire to clarify these phenomena and the underlying mechanisms, and considering that two-dimensional detonations have simpler transverse wave structures compared with three-dimensional ones, this study first conducted a numerical investigation of detonations propagating near the critical propagation state in two-dimensional channels filled with unstable mixtures. Subsequently, a shock polar theory is introduced based on several key assumptions, so as to predict and analyse the dynamics of the STW. This approach helps us better understand the nature of the transverse wave dynamics, thereby further elucidating the relationship between transverse wave structures and the MLE. Further, the differences between the first and second kinds of STW structures are assessed in conjunction with constant-volume combustion theory.

Because the detonation wave is inherently unstable and often in a critical state in practical applications, such as the assessment and prevention of industrial explosion hazards, as well as the operation of detonation-based propulsion devices, the relevant research can provide guidance for the fields of safety engineering and aerospace propulsion.

The remainder of the paper is structured as follows. The computational models used in this study are introduced in § 2. In §§ 3 and 4, the results of numerical simulations and theoretical analyses, along with their related discussions, are detailed. Finally, § 5 provides concluding remarks.

2. Computational models

2.1. *Governing equations*

The time-dependent reactive Euler equations are employed to numerically solve two-dimensional (2-D) gaseous detonation with convective and reactive effects, as follows:

$$\frac{\partial \boldsymbol{Q}}{\partial t} + \boldsymbol{\nabla} \cdot (\boldsymbol{F}) = \boldsymbol{S}, \tag{2.1}$$

where $\boldsymbol{Q}$, $\boldsymbol{F}$ and $\boldsymbol{S}$ represent the vector of conserved variables of the solution, the face flux vector corresponding to the conserved variables and the source vector, respectively. The details of these vectors are expressed as follows:

$$\boldsymbol{Q} = \begin{bmatrix} \rho Y_1 \\ \vdots \\ \rho Y_N \\ \rho \boldsymbol{U} \\ \rho E \end{bmatrix}, \quad \boldsymbol{F} = \begin{bmatrix} \rho Y_1 \boldsymbol{U} \\ \vdots \\ \rho Y_N \boldsymbol{U} \\ \rho \boldsymbol{U}\boldsymbol{U} + p \\ \rho E \boldsymbol{U} + \boldsymbol{U} p \end{bmatrix}, \quad \boldsymbol{S} = \begin{bmatrix} \omega_1 \\ \vdots \\ \omega_N \\ 0 \\ \omega_T \end{bmatrix}, \tag{2.2a-c}$$

where N is the total number of species, ρ is the total density of the mixture, $Y_k (k = 1, \ldots, N)$ is the mass fraction of the kth species, $\sum_{k=1}^{N} (Y_k) = 1$, $\boldsymbol{U} = (u_x, u_y, u_z)^{\mathrm{T}}$ is the velocity vector (u_y always equals zero for the 2-D case of present work), p is the pressure and E is the total energy without chemical energy, which is

calculated by

$$E = h_s - \frac{p}{\rho} + \frac{1}{2}\|\boldsymbol{U}\|^2. \tag{2.3}$$

The sensible enthalpy h_s in the above equation is evaluated by the seven-coefficient polynomial from the JANAF tables (Chase *et al.* 1975). The equation of state for a thermally perfect gas is utilized to close the system of governing equations. The source term ω_k of the kth species equation represents the formation/consumption rate of the kth species, and is determined by the law of mass action. The source term ω_T of the energy equation in (2.2) is the rate of reaction heat release, and is expressed as

$$\omega_T = \sum_{k=1}^{N} \omega_k \Delta h^{\circ}_{f,k}, \tag{2.4}$$

where $\Delta h^{\circ}_{f,k}$ is the formation enthalpy of the kth species.

2.2. *Numerical methods*

Based on an unstructured grid and finite volume framework, the adaptive mesh refinement framework available within OpenFOAM (Jasak 1996) is employed for discretizing the computational domain, and the refinement criterion is set based on the density gradient, which is an indicator of not only the shock wave but the contact discontinuity. The time terms in the governing equations are processed via a second-order total variation diminishing (TVD) RungeKutta scheme with the time step being dictated by the Courant–Friedrichs–Lewy (CFL) number, which is set to 0.3 for all computations undertaken in this study. The convection term $\boldsymbol{F}$ is approximated using a second-order central-upwind scheme (Kurganov, Noelle & Petrova 2001) that proficiently pinpoints the location of various discontinuities in the flow field. Hence, this scheme is widely used in the study of detonations (Gutiérrez Marcantoni *et al.* 2017; Guo *et al.* 2023). A detailed hydrogen combustion reaction mechanism (listed in Appendix A) proposed by Burke *et al.* (2012) is used to model the chemical reactions due to its special treatment of hydrogen combustion under high-pressure conditions. The source terms ω_k for the chemical reactions are solved using the Euler point-implicit method in the present study, effectively reducing the stiffness associated with the system of ordinary differential equations.

2.3. *Computational configurations*

To conduct the numerical simulation of the detonation wave in a 2-D channel, the shock-fixed frame is used, as shown in figure 2. We used two different mixtures, i.e. the stoichiometric H_2/air and the stoichiometric H_2/O_2 mixtures, and the computational conditions for both mixtures are listed in table 1. To understand the temperature sensitivity of the mixture, an effective activation energy ϵ was defined as

$$\epsilon = \frac{1}{T_s}\left(\frac{\ln t_{ig}^{+} - \ln t_{ig}^{-}}{\frac{1}{T_s^{+}} - \frac{1}{T_s^{-}}}\right), \tag{2.5}$$

where T_s is the post-shock temperature of the Chapman–Jouguet (CJ) detonation, $T_s^{\pm}$ is the perturbed post-shock temperature, $T_s^{\pm}$ is usually set to $(1 \pm 0.01)T_s$ (Lu *et al.* 2021)

Mixture	p_0 (kPa)	T_0 (K)	γ	M_{CJ}	ϵ	Δ_{ind} (μ m)
H_2/air(stoich.)	60	300	1.4	4.8	6.8	337
H_2/O_2(stoich.)	20	300	1.4	5.3	4.3	285

Table 1. Mixture conditions for initial computations. The effective activation energy ϵ and the induction zone length Δ_{ind} are solved by Shock-Detonation Toolbox (Browne *et al.* 2023).

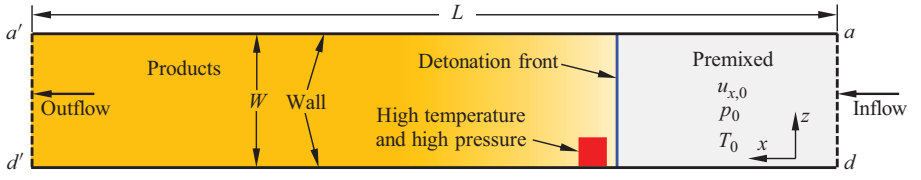

Figure 2. Computational configurations (shock-fixed frame) for 2-D channel.

and $t_{ig}^{\pm}$ is the ignition delay time (solved by the constant-volume combustion method) corresponding to a post-shock state with perturbed temperature.

Note that the two mixtures in table 1 belong to unstable gases, since their effective activation energies are relatively high. The stoichiometric H_2/air exhibits a higher effective activation energy, rendering it more sensitive to variations in temperature, while the stoichiometric H_2/O_2 possesses a higher CJ detonation strength, predisposing it to inducing stronger hydrodynamic instabilities. The addition of nitrogen dilution is to study the effect of activation energy on the stability of detonation wave propagation, that is, to examine the temperature sensitivity of detonation wave propagation. However, the impact of initial pressure on the temperature sensitivity can be ignored. Adjusting the pressure primarily aims to ensure that the detonation for the two mixtures propagates at a similar critical propagation state when the channel size is comparable. The implications of these parameter disparities will be analysed in the subsequent discussions.

The computational domain is a rectangle, as shown in figure 2. The right side of the computational domain is set as an inflow boundary for the gas mixture at pressure p_0 and temperature T_0, the inflow velocity has only an x direction and is fixed at the CJ detonation speed, i.e. $u_{x,0} = D_{CJ}$. The walls of the channel are adiabatic slip boundaries, and the left boundary condition of the computational domain is a zero-gradient outflow. The length L has been set to approximately 210 times the length Δ_{ind} of the induction zone (defined as the region between the von Neumann pressure front and the location of the heat release peak in a 1-D Zeldovich–von Neumann–Döring (ZND) structure under CJ detonation speed, that is, a CJ-ZND structure), with the aim to ensure that the flow is supersonic near the zero-gradient outflow boundary, thus the disturbances from the outflow boundary cannot influence the detonation front. Additionally, although the propagating speed of the detonation wave exhibits longitudinal oscillations during the simulations, it is found that the average propagating speed of the detonation wave is very close to the theoretical CJ speed so that the leading shock of the detonation wave does not move outside of the sufficiently long computational domain. Therefore, setting a constant value of the theoretical CJ speed at the inflow boundary condition is reasonable. For different computational cases, the width W of the computational domain or channel varies.

At the initial moment, the gas mixture under inflow conditions fills the area to the right side of the detonation front, whereas the area to the left side of the front is set to

have a CJ-ZND structure. A high-temperature, high-pressure squared area (indicated as the red box in figure 2), with a temperature of $10T_0$ and a pressure of $100p_0$, and a side length that equals the length of an induction zone, is artificially added downstream of the detonation front as an initial disturbance to facilitate the rapid generation of the transverse wave. A suite of tests with different computational grid sizes was conducted to minimize computational errors as much as possible, that might otherwise potentially influence the detonation, such as truncation errors and numerical oscillations (which are comparable to environmental noise in experiments, being both unavoidable and secondary). The details of the tests can be found in Appendix B.

3. Morphological evolution of transverse wave

3.1. *Propagation mode of 2-D detonation*

This section first investigates the influence of channel width on the propagation modes of detonation and the motion of the transverse wave. Figure 3 presents the numerical foils of high pressure within the channel for several typical channel widths, showcasing the detonation cell patterns under typical propagation modes. At first glance, it can be observed from figure 3(*a*) that, at small channel widths (i.e. $W = 0.5$ mm) for a stoichiometric H_2/air mixture, the detonation wave cannot leave continuous high-pressure tracks on the wall, indicating that transverse waves cannot continuously appear. This phenomenon exhibited by this mode has been reported in previous studies (Ishii & Grönig 1998; Sugiyama & Matsuo 2012; Tsuboi, Morii & Hayashi 2013). Sugiyama & Matsuo (2012) referred to the mode as the 'pulsed mode'. In this mode, the detonation wave primarily exhibits highly longitudinal instability, with transverse wave structures being influenced by the longitudinal pulsations, causing an intermittent appearance of the structure. It is considered that this paper focuses on the transverse characteristics of detonation, so the pulsed mode is not analysed in subsequent discussions.

As the channel width increases, the pattern of the half-cell is clearly displayed on the numerical foil, as shown in figure 3(*b*), indicating the presence of a transverse wave within the detonation. Because the transverse wave structure appears to guide the detonation forward like a head during propagation, the detonation mode shown in figure 3(*b*) is called as the single-headed mode (Kellenberger & Ciccarelli 2020). As the channel width further increases, a complete cell can exist within the channel (see figure 3*c*). At this point, the number of transverse waves in the detonation begins to change spontaneously. The mode with two transverse waves occupies a smaller proportion of the propagation process, with the detonation wave transitioning between single and dual transverse wave modes. Therefore, it is referred to as the single-dual-headed critical mode. Eventually, two transverse waves dominate the propagation of the detonation in the wider channel, as shown in figure 3(*d*). Thus, the detonation propagation mode at this situation is defined as the dual-headed mode.

Similarly, for a stoichiometric H_2/O_2 mixture, the detonation waves can also exhibit the aforementioned modes: the pulsed mode as shown in figure 3(*e*), the single-headed mode in figure 3(*f*), the single-dual-headed transition mode in figure 3(*g*) and the dual-headed mode in figure 3(*h*). Since H_2/air mixtures are less stable than $H_2/O_2{}'$ mixtures, the detonation cell pattern shown in figure 3(*d*) is more irregular compared with that in figure 3(*h*). Nonetheless, from a statistical average perspective (Lee *et al.* 1995), both belong to the dual-headed mode.

To explore the relationship between detonation modes and channel width in more detail, the propagation modes of detonation waves across various mixture conditions and channel

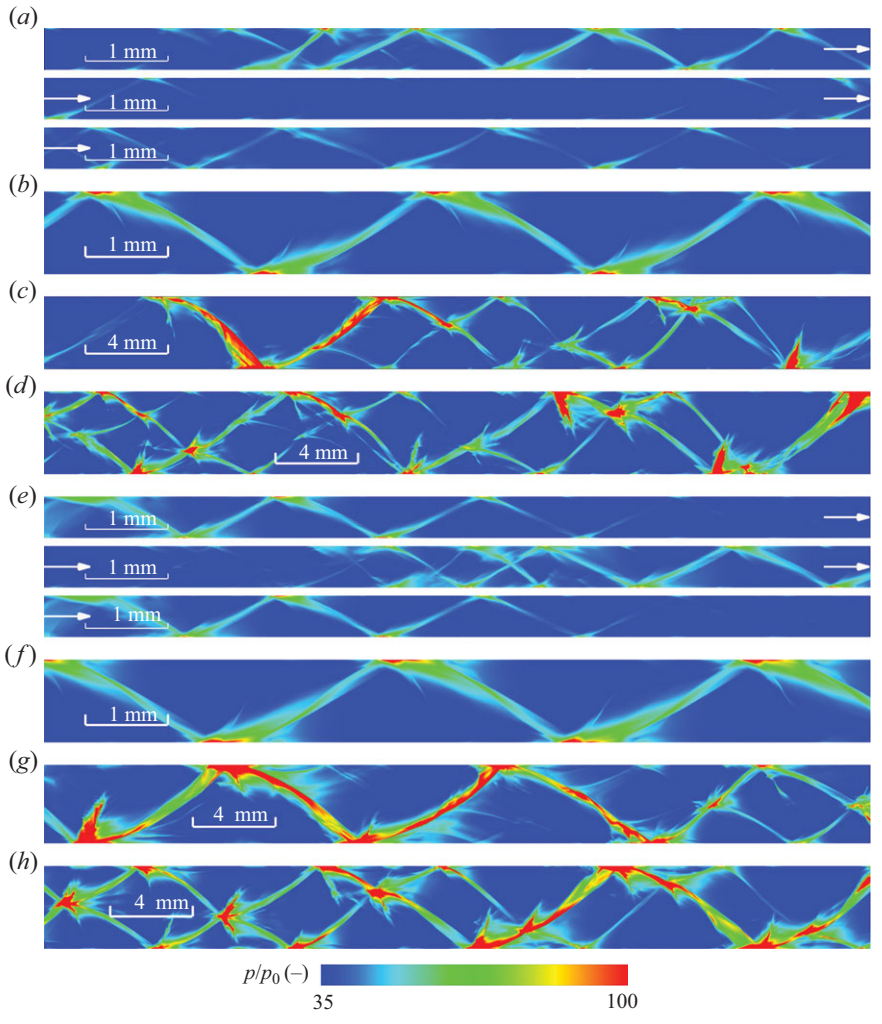

Figure 3. Numerical foils of high pressure in the 2-D domain of channel width $W =$ (*a*) 0.5 mm, (*b*) 1.0 mm, (*c*) 3.5 mm and (*d*) 4.0 mm with a stoichiometric H_2/air mixture, and $W =$ (*e*) 0.5 mm, (*f*) 1.0 mm, (*g*) 3.8 mm and (*h*) 4.0 mm with a stoichiometric H_2/O_2 mixture. Detonation front propagates from left to right.

widths are depicted in figure 4. Since the detonation cell size is largely related to the induction zone length (Ng, Ju & Lee 2007), the relationship between the detonation propagation modes and channel width for the two types of mixtures is generally consistent. Specifically, in figure 4, there is a region where all detonations propagate in a single-headed mode for two mixture conditions. Within this region, changes in channel width do not alter the propagation mode of the detonation wave, indicating that a mode-locking phenomenon or effect appears.

It should be noted that the channel width range required to sustain the MLE varies slightly for different mixture conditions. Upon inspecting table 1, the most significant difference between the two mixtures lies in their effective activation energies ϵ, which means the detonation sensitivities to temperature are different for the two mixtures. Due to the activation energy being able to affect the cell structure regularities

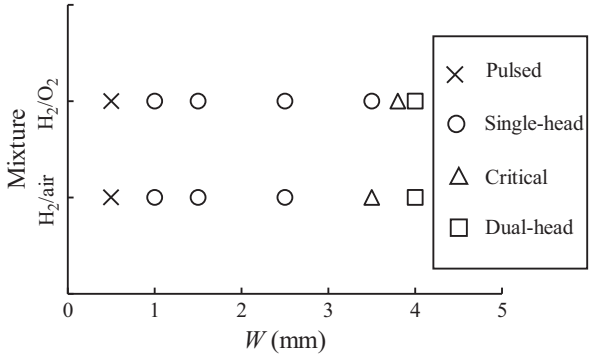

Figure 4. Detonation propagation modes under different mixtures and channel widths.

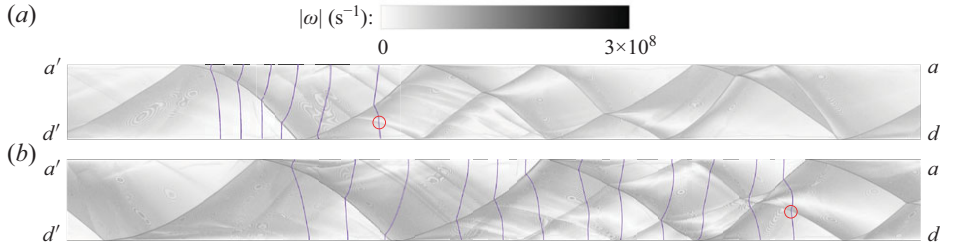

Figure 5. Numerical foils of vorticity for the critical mode in a 2-D domain with (*a*) $W = 3.5$ mm and stoichiometric H_2/air mixture and (*b*) $W = 3.8$ mm and stoichiometric H_2/O_2 mixture. The vorticity $|\omega|$ is calculated using $|\nabla \times (\boldsymbol{U})|D_{ref}/D_{CJ}$, where D_{ref} is the reference speed, which is set to 2000 m/s in this paper. The detonation wave indicated by the purple line propagates from left to right.

(Lu *et al.* 2021; Zadok *et al.* 2023), the difference leads to different critical channel widths at which the number of transverse waves is shifted during the detonations.

3.2. *Generation of transverse waves*

To understand how triple points on the wave front are generated and how the detonation waves detach from the MLE when the channel width increases, figure 5 provides numerical foils of vorticity under the critical mode conditions for both mixtures. It is evident that, during the critical mode, there is a transition in the detonation wave from single-headed to dual-headed patterns (the new fully developed triple points are circled in red in figure 5). Accordingly, several typical moments have been selected (the detonation fronts at typical moments are indicated by purple lines) for the analysis of the detonation flow field, and to observe the origin of transverse waves.

To clearly demonstrate the entire process of transverse wave creation in the detonation, the temperature and pressure gradient distributions in the detonation flow field (at six different times consisting of the purple lines in figure 5*a*) within a channel of $W = 3.5$ mm filled with stoichiometric H_2/air are presented in figure 6. At $t = 93.6$ µs, there is only one triple point, TP1, on the front, where the transverse wave (see TW1 in figure 6) has begun to propagate from the upper wall towards the lower wall after reflection. During the collision of the transverse wave with the upper wall, a local explosion occurs, and thus induces a local overdriven detonation in the vicinity of the unreacted gas pocket, resulting in the formation of two forward explosion waves (FEWs) and two backward

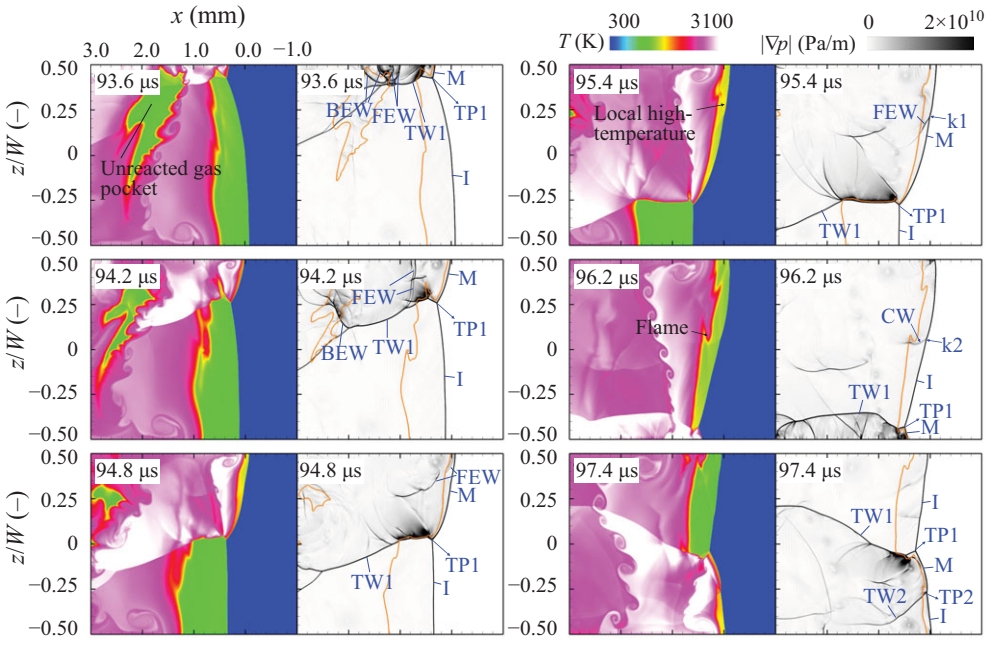

Figure 6. The temperature and pressure gradient distributions of the detonation flow field at different times in the channel of $W = 3.5$ mm filled with stoichiometric H_2/air mixture. The orange lines represent reaction surfaces of $Y(O_2) = 0.118$: FEW – forward explosion wave, BEW – backward explosion wave, TW – transverse wave, CW – compression wave, TP – triple point, M – Mach front and I – incident front.

explosion waves. As time progresses to $t = 94.2$ μs, two FEWs gradually approach each other and subsequently merge into a single FEW. Due to the flow velocity and the acoustic impedance (or temperature) being uneven behind the Mach front, only part of the FEW passes through the reaction surface and approaches the Mach front at $t = 94.8$ μs. Next, the interaction of the FEW with the Mach front produces a kink marked by k1 on the Mach front at $t = 95.4$ μs. This interaction strengthens the Mach front above k1, which in turn increases the temperature of fluid behind the front. Since the stoichiometric H_2/air mixture is quite sensitive to temperature, the increase in flow field temperature induces a bulge flame on the reaction surface, as shown in the flow field at $t = 96.2$ μs. The flame accelerates and subsequently generates a compression wave (CW). This CW interacts with the detonation front to create a kink k2, which continues to propagate toward the lower wall. After the interaction between k2 and TP1, k2 passes through TP1, evolves into a new triple point TP2 and induces the transverse wave TW2. Ultimately, there are two triple points, TP1 and TP2, on the detonation front in the flow field, and the MLE fails.

In essence, the creation of a new full developed TP undergoes in three stages. First, a FEW interacts with the Mach front, altering the strength of the Mach front. Second, a local bulge flame develops on the reaction surface due to the change in strength of the Mach front. Third, the bulging flame accelerates and induces a CW, which then interacts with the detonation front to form a new TP. The underlying cause of this sequence is a localized overdriven detonation at a spot with unreacted gases, triggered by a localized explosion. The effect of unreacted gas has also been mentioned in 1-D detonation studies (Sharpe & Falle 2000; Daimon & Matsuo 2007). The explosion wave generated in an unreacted gas pocket can strengthen the 1-D detonation front, so as to maintain its propagation. However, the study of the impact of this explosion wave on multi-dimensional detonation fronts is

still relatively limited. This paper presents a novel mechanism of generation of transverse waves that has not been fully explained before.

Similarly, figure 7 displays the temperature and pressure gradient distributions in the detonation flow field within a channel of $W = 3.8$ mm for a stoichiometric H_2/O_2 mixture, at twelve different times consisting of the purple lines in figure 5(*b*). At $t = 29$ μs after the collision between TP1 and the upper wall, the transverse wave reflects off the upper wall and propagates towards the lower wall. During the collision process, a forward jet is induced. This jet, with its strong impact force, interacts directly with the Mach front, causing the Mach front to bend at a point marked as k1. In a previous study (Mach & Radulescu 2011), the aforementioned process is referred to as Mach reflection bifurcation (belonging to hydrodynamic instability). As time progresses, k1 gradually evolves into a distinct TP. Since the transverse wave induced by this TP has not yet fully developed, it is referred to as a WTP (see the WTP1 in the flow field at $t = 29.8$ μs). As shown in the flow fields at $t = 30.6$ μs and 31.6 μs, the wave system around WTP1 interacts with the reaction surface, causing it to become unstable. This instability makes the formation of a series of CWs, which subsequently interact with the detonation front, resulting in the generation of WTP2 and WTP3.

During their downward propagation, WTP1 and WTP2 interact with TP1, which propagates upward after reflection on the lower wall; WTP1 and WTP2 pass through TP1. This interaction strengthens WTP1 and WTP2. Simultaneously, the increase in temperature behind WTP1 and WTP2 makes the fluid particles in their vicinity more reactive, which in turn benefits the sustenance of WTP1 and WTP2. At $t = 31.6$ μs, k2 is also generated by the interaction of the forward jet with the detonation front. When the time reaches $t = 32.2$ μs, WTP1 and WTP2 and k2 coalesce to form WTP4. Simultaneously, WTP3 interacts with TP1 and passes through it, leading to an enhancement of WTP3. Also, WTP4 reflects off the lower wall and moves towards WTP3, as shown in the pressure gradient distribution at $t = 32.8$ μs. Until $t = 33.6$ μs, the downward-propagating WTP3 and the upward-propagating WTP4 interact and penetrate each other. This interaction leads to an increase in the local fluid temperature, which in turn gives rise to a bulging of the reaction surface. Additionally, TP1 reflects off the upper wall and propagates downward, the k3 also appears after the action of a forward jet.

For the flow field at $t = 34.2$ μs, WTP4 interacts with TP1 and passes through it, and WTP4 is further strengthened. At this time, k3 evolves into a weaker WTP5, while WTP3 reflects off the lower wall and propagates upward. As time proceeds, WTP4 continues to propagate upward, while WTP5 gradually weakens and eventually dissipates due to interactions among the wave systems. At $t = 35.0$ μs, WTP3 just interacts with TP1, and they pass through each other, further strengthening WTP3. By $t = 35.6$ μs, WTP3 maintains its propagation upward, coincidentally as TP1 just reflects off the lower wall and also moves upward. After colliding with the upper wall, WTP4 travels towards WTP3. At $t = 36.4$ μs after WTP3 and WTP4 interact, the fluid around them collides, creating an obvious high-temperature and high-pressure (HT and HP) region. Thus, this causes WTP3 and WTP4 to pass through each other, and the fluids of the HT and HP region propel WTP3 and WTP4 to propagate upward and downward, respectively. Lastly, WTP4 passes through TP1, and the transverse wave induced by WTP4 fully develops into TW2, thereby transforming WTP4 into TP2. Meanwhile, the upward-propagating TP1 engulfs WTP3. Consequently, there are now two TPs, TP1 and TP2, on the entire detonation front, indicating the failure of the MLE.

In summary, in the scenario of detonation in the channel filled with a stoichiometric H_2/O_2 mixture, the primary reason for the generation of a new fully developed transverse wave is the Mach reflection bifurcation. As mentioned earlier and in previous works

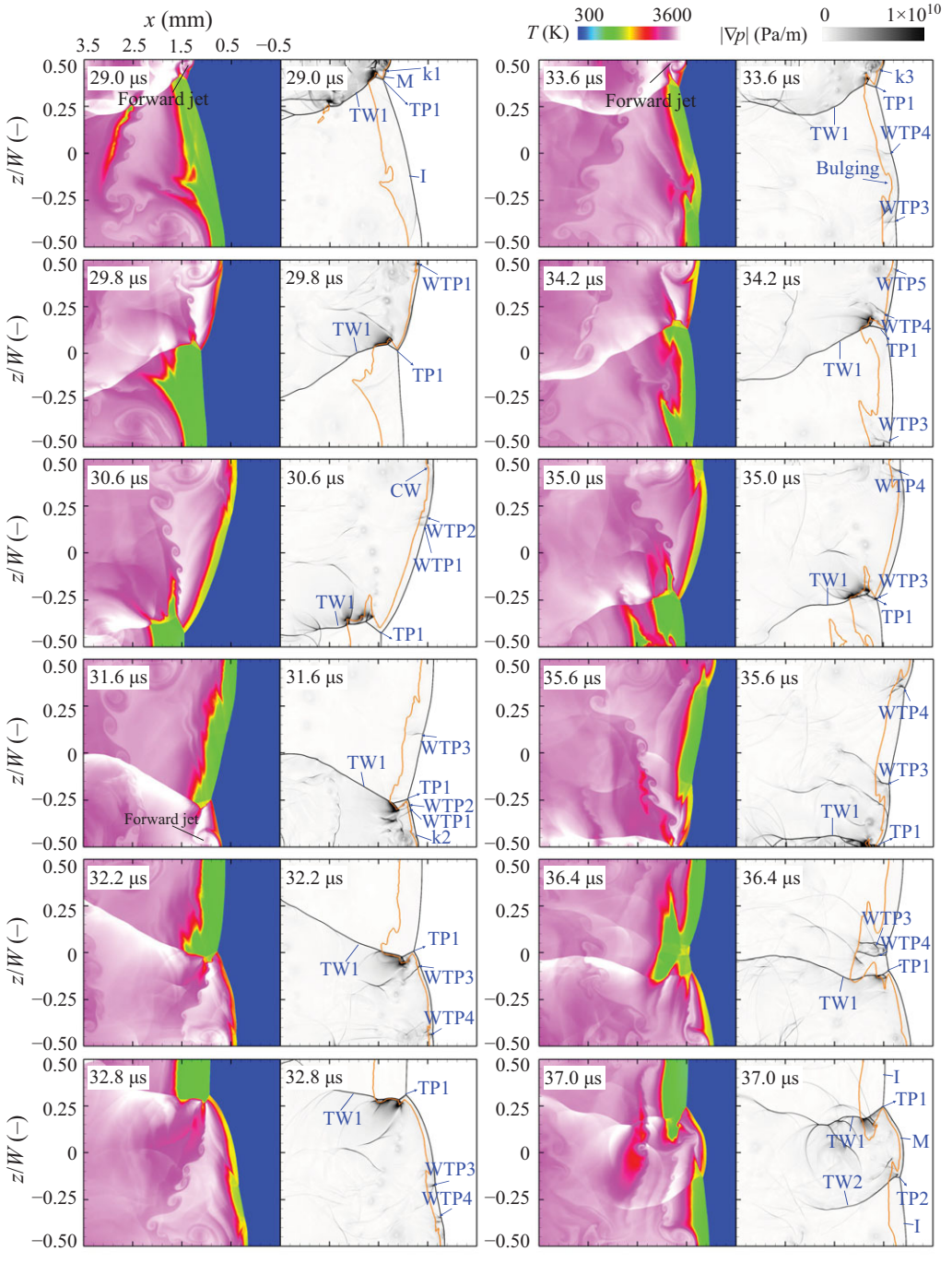

Figure 7. The temperature and pressure gradient distributions of the detonation flow field at different times in the channel of $W = 3.8$ mm with stoichiometric H_2/O_2 mixture. The orange lines represent reaction surfaces of $Y(O_2) = 0.4$: k – kink, TW – transverse wave, CW – compression wave, TP – triple point, WTP – weak triple point, M – Mach front and I – incident front.

(Semenov, Berezkina & Krassovskaya 2012; Shi *et al.* 2019), this bifurcation is caused by the forward jet, which is a manifestation of the flow non-uniformity within the flow field. Previous studies (Mach & Radulescu 2011; Lau-Chapdelaine, Xiao & Radulescu 2021; Sow, Lau-Chapdelaine & Radulescu 2021) have primarily relied on single-step global reaction models to investigate this process. However, the present paper is the first to thoroughly explore the generation of TPs caused by Mach reflection bifurcation based on real reactive system. Despite the use of different models, there is considerable qualitative consistency among them. Detailed analyses in this paper helps to deepen the understanding of the complex dynamics and interactions of detonation waves.

Notably, both failure mechanisms occur due to inherent instabilities within the detonation process. For detonations in stoichiometric H_2/air mixtures, the greater intrinsic chemical instability (higher effective activation energy) makes unreacted gas pockets more prone to forming localized explosion waves, leading to the failure of the MLE. In contrast, for detonations in stoichiometric H_2/O_2 mixtures, the stronger intrinsic flow instability (evidenced by higher detonation Mach numbers) causes bifurcations in the Mach front during Mach reflection, resulting in a failure of the MLE. For the failure mechanism of the MLE in H_2/air detonations, the interaction between explosion waves and the detonation front as a mechanism for cell growth is emphasized, which is not considered in previous studies.

3.3. *Influence of channel width on mode locking*

The above subsection indicates that the failure mechanisms of MLE for the two mixtures are distinctly different. This is consistent with the differences in channel width for the critical modes mentioned earlier, which are attributed to differences in the effective activation energies of the mixtures (i.e. their different temperature sensitivities). Although the MLEs fail in different ways for both mixtures, the failure is caused by changes in the channel width. However, it is not clear what influence the variation in channel width has on propagation of detonation waves, in other words, why would variation in channel width cause the MLE to fail?

To address the question mentioned above, here, we focus on the effects of channel width on detonation waves under the MLE, specifically in a single-headed mode. Figure 8 presents the variation over time of the longitudinal speed of the single-headed detonation wave fronts on the lower wall of the channel for different channel widths. Clearly, all the front speed curves exhibit highly periodic oscillation characteristics with period T_d. Nevertheless, the average speed of the detonation wave front primarily tends towards the theoretical CJ speed.

There are many jump features on the curves of figure 8, where the remarkable jump features are all generated by the collision of the front's TPs on the lower wall. In figure 8(a) with $W = 1.0$ mm, the collision causes the detonation front speed to jump from approximately $0.85D_{CJ}$ to approximately $1.25D_{CJ}$, with a step magnitude of $0.40D_{CJ}$. In the channel width of $W = 1.5$ mm, there is a jump from $0.80D_{CJ}$ to $1.35D_{CJ}$ shown in figure 8(b), with a step magnitude of $0.55D_{CJ}$, and the step magnitude has become larger. As the channel width further increases, the average step magnitude exceeds $0.6D_{CJ}$, further suggesting the influence of channel width. Likewise, for the detonation of stoichiometric H_2/O_2 mixture, increasing the channel width also increases the step magnitude. For example, in figure 8(d) with $W = 1.0$ mm, the magnitude is approximately $0.40D_{CJ}$, while in figure 8(e,f) with $W = 2.5$ mm and 3.5 mm, the magnitudes are roughly $0.65D_{CJ}$ and $0.80D_{CJ}$, respectively. Potentially, the increase in instantaneous strength contributes to the failure mechanism of the MLE described earlier.

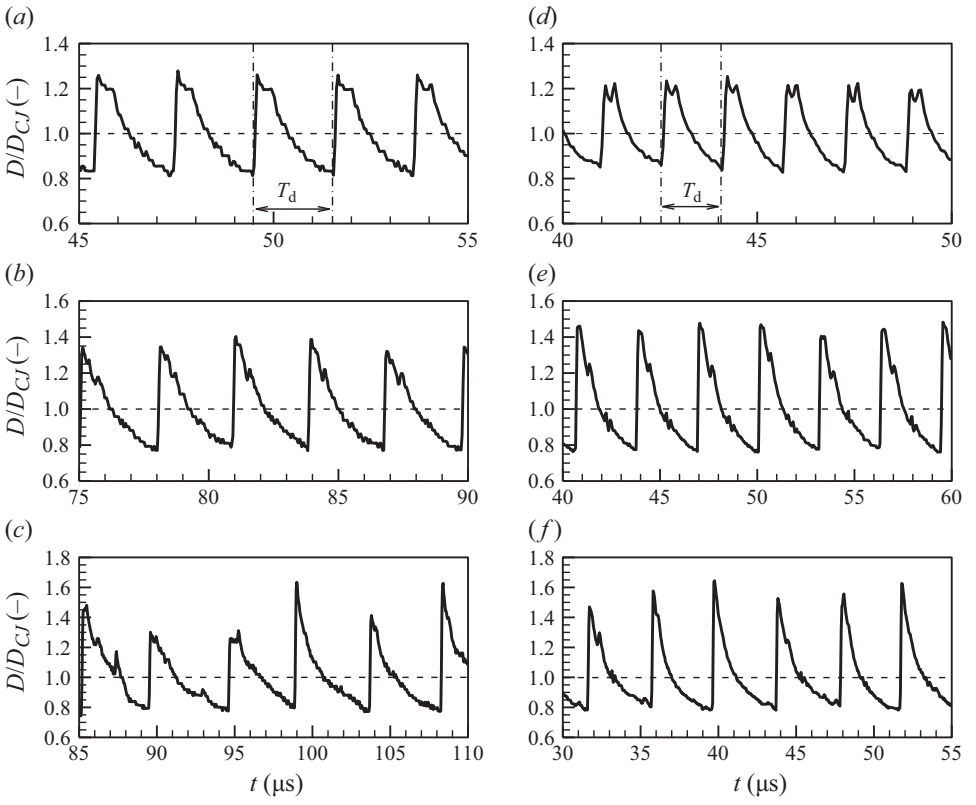

Figure 8. Dimensionless longitudinal speed of detonation wave front as a time function on lower wall of $W = (a)$ 1.0 mm, (b) 1.5 mm and (c) 2.5 mm filled with a stoichiometric H_2/air mixture, and $W = (d)$ 1.0 mm, (e) 2.5 mm and (f) 3.5 mm filled with stoichiometric H_2/O_2 mixture. The dashed line indicates the CJ detonation speed.

In fact, the period T_d in figure 8 represents the time interval at which TP acts between on both walls under a single-headed detonation mode. In view of this, figure 9 presents the curve of the period T_d along with variation of channel width. It can be seen that the period T_d increases approximately linearly with the channel width. This period also reflects the duration of the Mach front of the detonation wave. Since fluid particles behind the Mach front are more likely to react, a longer-life Mach front promotes the formation of new fully developed TPs.

On the other hand, since transverse waves or TPs traverse a distance of double channel widths in one period, the average transverse wave speed $\overline{D}_Z$ (laboratory frame) can be obtained through $2W/T_d$. This average speed represents the motion characteristics of transverse waves in transverse space. To understand the impact of channel width on the motion of transverse waves, the diagrams of the average transverse speed of transverse waves versus channel width in a single-headed detonation scenario for both mixtures are shown in figure 10(a,b). One can see from figure 10 that the average transverse speed of the TPs increases as the channel width increases for both mixtures. This implies that the transverse motion of the transverse wave in the detonation becomes stronger for a wider channel. Since the explosion wave and Mach reflection, as described earlier, both originate from the collision of the transverse wave on the wall, stronger transverse motion

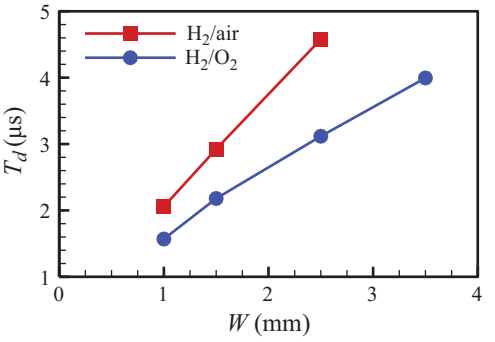

Figure 9. Period of interaction between the TP and the wall dd'.

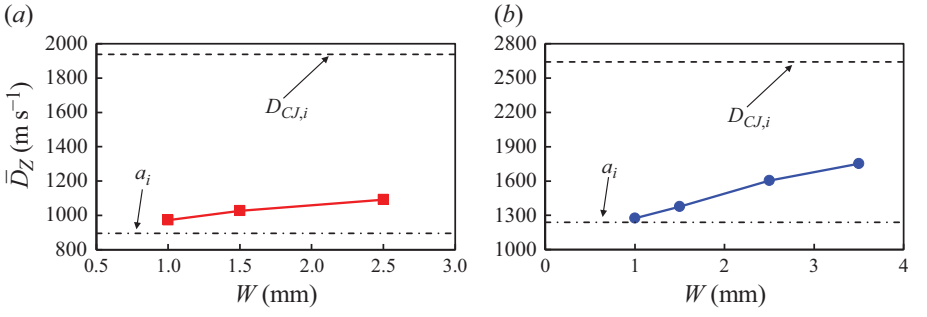

Figure 10. Average transverse speed of TP under (*a*) stoichiometric H_2/air and (*b*) stoichiometric H_2/O_2 mixtures as functions of channel widths. Here, $D_{CJ,i}$ and a_i are the CJ detonation speed and the speed of sound in the induction zone, respectively, calculated based on the post-shock states of the 1-D steady-state CJ-ZND structure.

of transverse wave structures is necessary to trigger strong explosion waves or Mach reflection.

To summarize, increasing the channel width not only intensifies the explosion waves and Mach reflections arising from the collision of transverse wave on the wall but also extends the time interval between two collisions. These changes make the reaction surface more susceptible to destabilization and allow more time for the destabilized reaction surface to develop, thus causing the MLE to fail ultimately. On the other hand, when the channel width is too small, transverse wave structures cannot exist continuously; that is, TPs appear intermittently (see figure 3*a*,*e*) or do not appear at all (see the work of Chinnayya, Hadjadj & Ngomo 2013). According to figure 10, it can be inferred that, under extremely small channel width conditions, the transverse wave structure with an average transverse speed slightly greater than or close to the induction zone's sound speed is not allowed to constantly exist within the flow field, thereby the failure of the MLE is caused by a different way. The specific reasons are discussed in subsequent sections.

3.4. *Details of transverse wave structure*

The detonation modes described in the above sections are closely related to transverse wave (TW) structure. Particularly, the appearance and transverse motions of the TW structure affect the MLE. Therefore, it is necessary to deepen study the TW structure of the detonation.

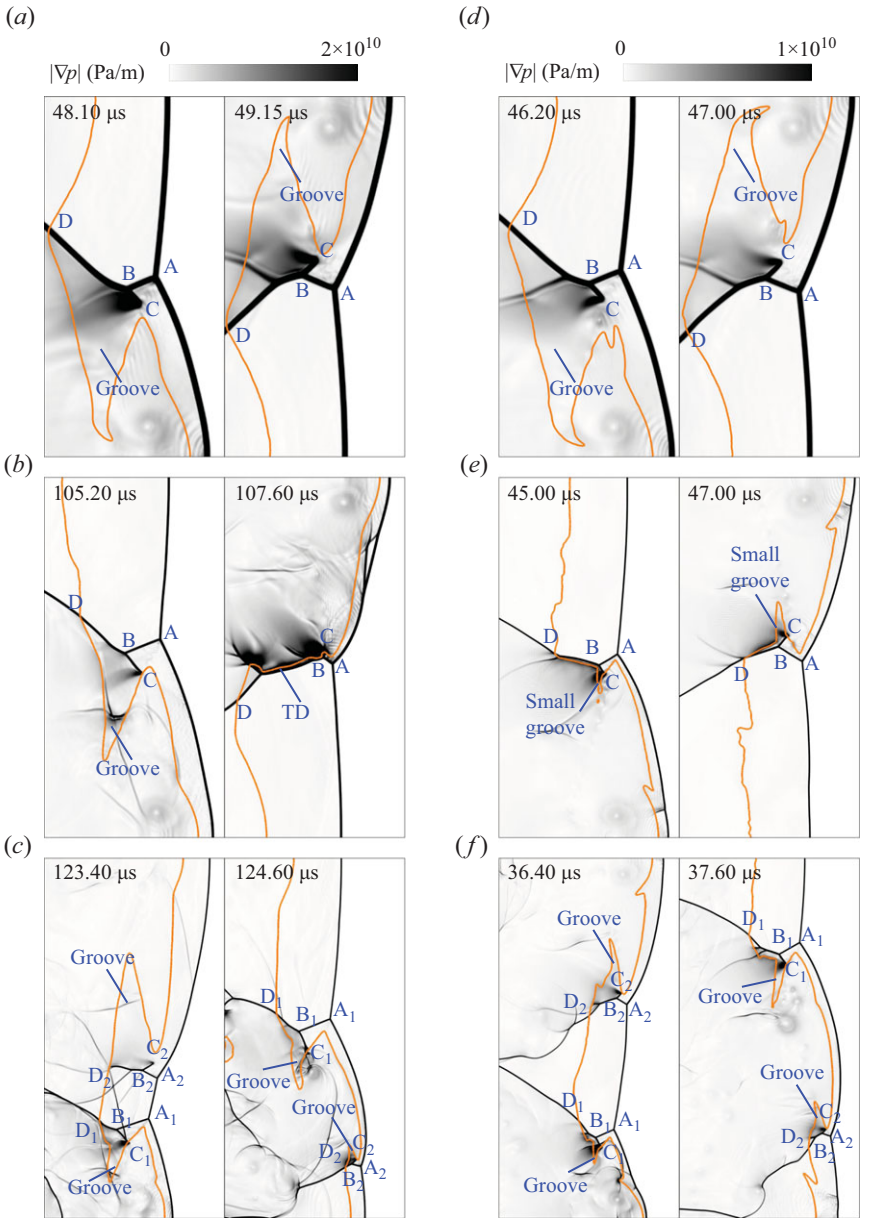

Figure 11. Shock waves indicated by high pressure gradient and reaction surfaces given by the isoline of $Y(O_2) = 0.118$ (left) or $Y(O_2) = 0.4$ (right) in the channel of $W =$ (*a*) 1.0 mm, (*b*) 2.5 mm and (*c*) 4.0 mm with stoichiometric H_2/air mixture, and $W =$ (*d*) 1.0 mm, (*e*) 3.5 mm and (*f*) 4.0 mm with stoichiometric H_2/O_2 mixture. For each snapshot, its height represents the full channel width, and the aspect ratio in both horizontal and vertical directions is 1:1.

Figure 11 displays the shock structures and reaction surfaces for different mixtures at different channel widths, represented by pressure gradient distributions overlapped by contours of species O_2. Clearly, the TW structures in detonations studied in this paper all belong to STW structures, which are characterized by the presence of two TPs, designated as A and B, near the detonation front. This structure is consistent with the schematic

shown in figure 1, illustrating the ubiquity of STW structures. When conditions are near the threshold of the critical propagation state, at 48.10 μs and 49.15 μs displayed in figure 11(*a*), a distinct unreacted gas groove is present near the STW structures in the flow field, indicating that the STW structures under this condition are of the second kind defined as figure 1(*b*). As the channel width increases, the structure of the TWs is affected. It can be seen that there are differences in the flow field near the strong structures in figure 11(*b*). At 105.20 μs, a pronounced groove is present in the flow field, indicating that the TW structure at this time is of the second kind of STW structure. While at 107.60 μs, a TD wave completely replaces the groove, transforming the TW structure into a first kind of STW structure. This significant difference is primarily due to the fact that stoichiometric H_2/air mixtures are relatively unstable. However, as shown in figure 10(*a*), the average transverse speed of the TWs under the condition of figure 11(*b*) is much lower than the CJ detonation speed, so it can be inferred that the occurrence of such TD that exits in the first kind of STW structure is relatively difficult in 2-D detonation. As a result, the TW structure is mainly dominated by the second kind of STW structure. When the detonation propagates in the wider channel shown in figure 11(*c*), there are two STW structures (indicated by TPs A_1 and A_2) in the flow field, with unreacted grooves around them. This again indicates that the second kind of STW structure is a more fundamental feature of 2-D detonations.

For a stoichiometric H_2/O_2 mixture, the TW structure of the detonation wave propagating when conditions approach the threshold of the critical propagation state also features the second kind of STW structure with unreacted gas grooves, as shown in figure 11(*d*–*f*). For such a relatively stable mixture, as the channel width increases, the unreacted groove region becomes small. However, even though the groove area has decreased, the transverse average speed of the structure (approximately $0.6D_{CJ}$) shown in figure 10(*b*) is significantly lower than the CJ detonation speed, indicating that TD is difficult to occur. This means that the entire TW structure still falls under the category of the second kind of STW structure. Furthermore, for the dual-headed mode of the H_2/O_2 mixture shown in figure 11(*f*), the TWs also clearly show the second kind of STW structures. Totally, the second kind of STW structure plays a predominant role in the 2-D detonations of the present work.

To further observe the relationship between the transverse motion and the flow field structure, figure 12 presents the variation over time in the transverse instantaneous speeds $|D_Z|$ of the TPs under a single-headed detonation mode. In one period, there are two stages in which the transverse speed gradually increases to cross a_i for all curves in figure 12, where the TP of first stage is from the lower wall to the upper wall, and the TP of second stage is from the upper wall to the lower wall. For the H_2/air detonation at $W = 1.0$ mm (figure 12*a*), the instantaneous transverse speed of the TP is overall much smaller than the CJ detonation speed, which implies that the TD is unlikely to appear in the flow field. As can be seen from figure 11(*a*), there exists a significant unreacted groove in the flow field without the presence of the TD, indicating that the flow field is dominated by the typical second kind of STW structure. For the detonation of such unstable gases as H_2/air mixtures, a wider channel allows more space and time for the development of detonation instability. Under the influence of this instability, the transverse speed exhibits chaotic characteristics, accompanied by abrupt acceleration in transverse speed, as illustrated in figure 12(*b*). This abrupt change in transverse speed can cause the speed value to approach the CJ detonation speed, thus enabling the development of TD in the flow field. However, from a statistical perspective (see figure 10*a*), the average transverse speed of the TP is significantly lower than the CJ detonation speed, which means that such sudden accelerations and the subsequent appearance of TDs are relatively rare, thus the flow field predominated by the second kind of STW structure is considered.

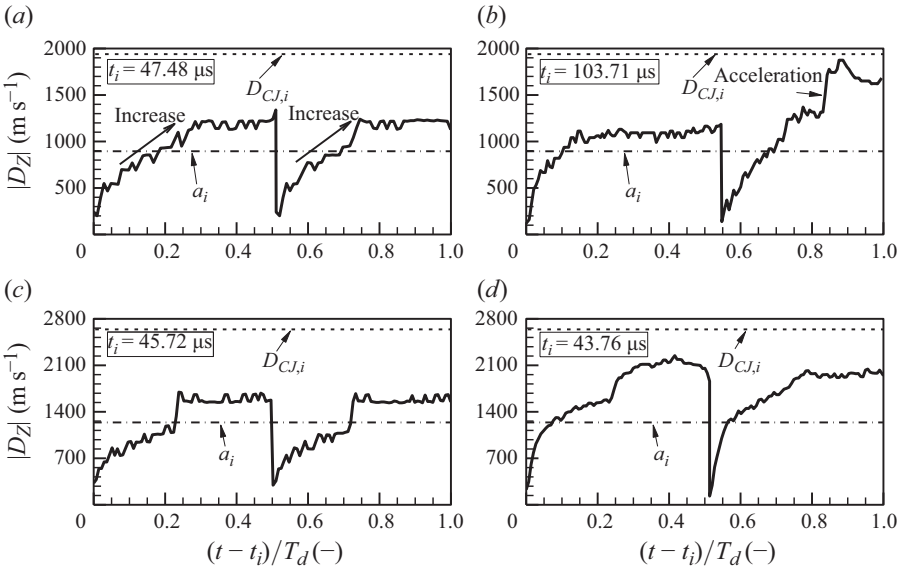

Figure 12. Transverse instantaneous speeds of the TPs as a function of time in the channel of $W =$ (*a*) 1.0 mm and (*b*) 2.5 mm filled with stoichiometric H_2/air mixture, and $W =$ (*c*) 1.0 mm and (*d*) 3.5 mm filled with stoichiometric H_2/O_2 mixture. Here, $D_{CJ,i}$ and a_i are the CJ detonation speed and the speed of sound in the induction zone, respectively, calculated based on the post-shock states of the 1-D steady-state CJ-ZND structure.

Similarly, when the channel width is relatively small, the transverse speed of the TP in a single-headed H_2/O_2 detonation is also much lower than the CJ detonation speed (see figure 12*c*), indicating that the TW intensity is weaker and the flow field exhibits the typical second kind of STW structure shown in figure 11(*d*). Particularly, for the wider channel of figure 12(*d*), due to the relative stability of the detonation in this mixture, the transverse speeds in both the first and second stages increase overall more smoothly. Compared with H_2/air detonations, this trend is more orderly. It can be seen that widening the channel results in an overall increase in the transverse speed of the TP in a single-headed H_2/O_2 detonation. Correspondingly, under the condition of figure 11(*d*), the unreacted groove is smaller but observable. Hence, the TW structure of the flow field is considered to be a second kind of STW structure. However, the quantitative relationship between the transverse speed and the size of the groove is currently unknown, thus necessitating theoretical analysis.

The above results indicate that the second kind of STW structure is more important and prevalent in 2-D detonations for both H_2/O_2 and H_2/air mixtures. It is noted that, as the channel width decreases, the maximum instantaneous transverse speed (as shown in figure 12) of the TP is reduced. It is evident that, in extremely narrow channels, the transverse speed of the TW near the wall cannot increase to a sufficient value, which prevents the maintenance of the STW structure and leads to the failure of the MLE. The factors for maintaining the STW structure are quantitatively analysed in § 4.

When the TWs approach the situation of TP disappearance (i.e. under $W = 1.0$ mm), the average transverse speed of the STW structure is very close to a_i, as shown in figure 10. Actually, a typical second kind of STW structure that just meets the speed of sound condition exhibits an acoustic coupling characteristic. To further recognize this acoustic coupling characteristic of the structure, figure 13 shows the wave structures of

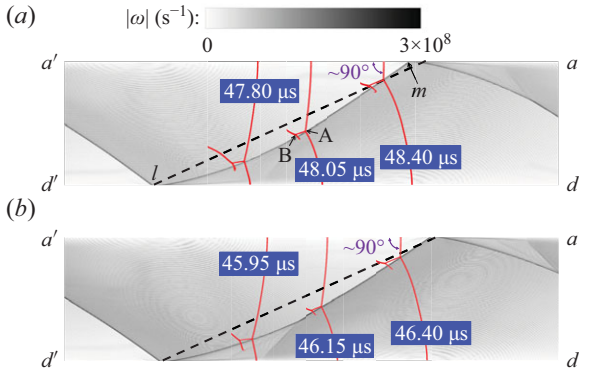

Figure 13. Numerical foils of vorticity and wave structures near detonation front in the 2-D domain of $W = 1.0$ mm filled with (*a*) stoichiometric H_2/air and (*b*) stoichiometric H_2/O_2 mixtures. The vorticity $|\omega|$ is calculated using $|\nabla \times (\boldsymbol{U})|D_{ref}/D_{CJ}$, where D_{ref} is the reference speed, which is set to 2000 m/s in this paper. The black dashed line indicates the trajectory of an acoustic wave in the induction zone of CJ-ZND structure.

different times and the numerical foil of vorticity in the 2-D domain of $W = 1.0$ mm with two mixtures. Obviously, during the upward movement of the TP, the TW structure is consistently "strong" type (Mahmoudi & Mazaheri 2015), moreover corroborating the importance of the STW structure. The black slim lines composed of higher vorticity on the foil of vorticity accurately indicate the movement trajectory of the TP A on the detonation front since the value of vorticity around A is larger. When the slim line segment appears like a left slash, as with segment lm, it represents the TP moving from bottom to top; otherwise, the TP moves in the opposite direction. The trajectory of the acoustic wave, indicated by the black dashed lines in figure 13, closely coincides with the trajectory of the TP for the two mixtures. This further demonstrates that a typical second kind of STW structure exhibits acoustic coupling characteristics. It is noteworthy that the aforementioned acoustic coupling characteristic in 2-D detonation is unusual, as previous literature (Fay 1952; Sugiyama & Matsuo 2013) has primarily addressed acoustic coupling in the context of a typical first kind of STW structure.

4. Analysis of transverse dynamics

Given the prevalence and importance of the second kind of STW structure, it is essential to study the detailed characteristics of the flow field around this structure. When approaching the critical propagation states ($W = 1.0$ mm for both mixtures), the flow fields of 2-D detonations consistently exhibit the typical second kind of STW structures (see figure 11*a*,*d*), accompanied by acoustic wave coupling features. The geometric configuration of the wave structure simulated numerically in such conditions remains relatively steady, and an analysis of the STW structure of the flow field can be carried out in a unified way.

Figure 14 provides the fields of species O_2 and pressure overlapped by TW shape around point A for a stoichiometric H_2/air mixture at a typical time $t = 48.05$ μs to elaborate on the characteristics of the flow field. At this moment, the TW structure is close to the central axis of the channel and is considered a standard second kind of STW structure. It can be observed that there is a HP region inside the STW structure. The movement of the HP region forms the numerical foils of HP, as shown in figure 3. Because this HP region

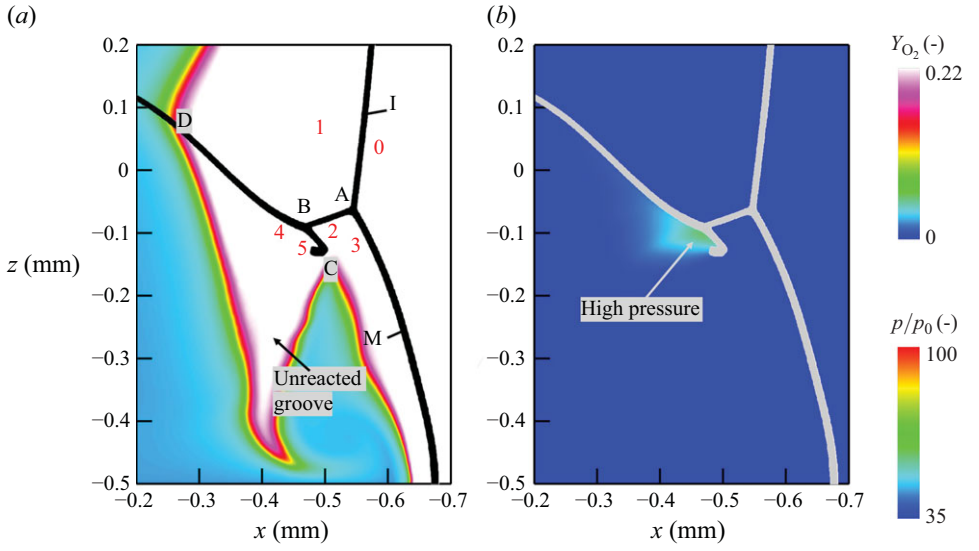

Figure 14. The fields of (*a*) species O_2 and (*b*) pressure overlapped by the shock waves around point A at $t = 48.05$ μs for detonation of a stoichiometric H_2/air mixture with $W = 1.0$ mm. The numerical symbols represent the different flow regions.

is closely behind the TW and thus demonstrates the dynamics of the TW structure, it is necessary to find a relevant theory to predict the value of HP. The detonation characteristics described in this section are also applicable to those of a stoichiometric H_2/O_2 mixture, so only the analysis for stoichiometric H_2/air mixture is provided here.

Figure 15, based on figure 14, illustrates the geometric schematic of flow field around TP A. Under a laboratory frame, the track angle α in figure 15(*a*) indicates the angle between the motion direction of TP A and a horizontal line, and can be determined by

$$\alpha = |\arctan(D_Z/D_X)|\,, \tag{4.1}$$

where D_X and D_Z are the longitudinal and transverse speeds of TP A, respectively. Here, D_A is the total speed of TP A. In a system where TP A is stationary (see figure 15*b*), the incoming flow velocity is expressed as $V_{(0)} = D_X/\cos(\varphi)$, where φ is the incoming flow angle relative to the horizontal baseline, and is equal to α. The velocity of the fluid particle in the ξ-direction is determined by $u_\xi = u_x - D_{CJ} + D_X$ (since the fixed-shock frame is defined by the CJ plane detonation wave), while the velocity of the fluid particle in the η-direction is defined as $u_\eta = u_z - D_Z$. Indeed, the TW structure causes multiple deflections on the fluid flow around TP A. Note that $\theta_{(i)}(i = 1, \ldots, 5)$ is the total flow deflection angle of ith flow state, which is always the angle between the current flow direction and the incoming flow direction. The front angle χ_I is defined as the angle between the incident front and the baseline. Similarly, the front angle χ_M is the angle between the Mach front and the same baseline, as shown in figure 15(*b*). The shock wave angle β is the angle between the current shock and the flow direction ahead of it. Specifically, there exists a relationship between the front angle and shock wave angle. For the incident front, $\beta = \chi_I - \varphi$, while for the Mach front, $\beta = 180° - \chi_M - \varphi$. At this point, the geometry of the flow field structure has been fully defined.

Considering that the detonation morphologies discussed in § 3 are related to the flow state of the fluid, where the pressure conditions in the flow field and the movement of TWs reflect the transverse dynamic characteristics of the detonation, it is necessary to

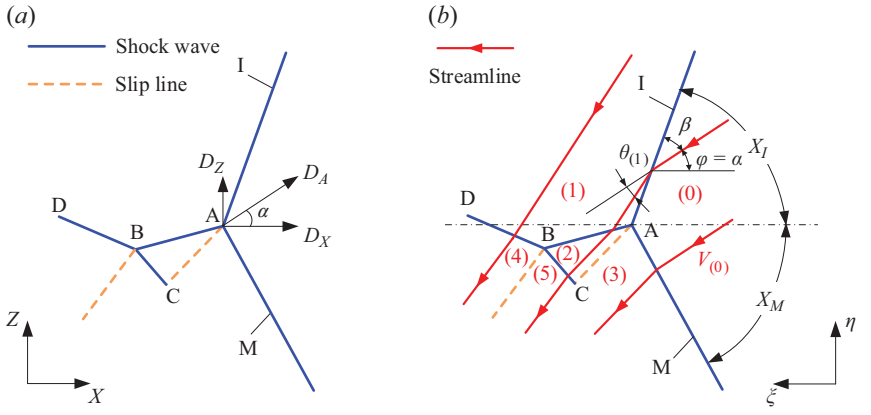

Figure 15. The sketches of flow field around point A of the STW structure in the (a) laboratory frame and (b) TP A frame. The numerical symbols represent the different flow regions.

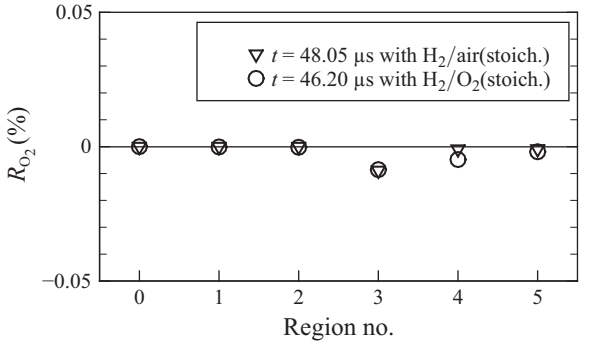

Figure 16. The relative change of Y_{O_2} at the different regions around the STW structure in the channel of $W = 1$ mm.

understand the relationship between the evolutions of the wave structure and the transverse dynamics. This section conducts the analysis of the STW structure based on the shock polar theory, due to the detonation flow field exhibiting a series of classical features of shock reflection. Figure 16 presents the distribution of relative change (R_{O_2}) of oxygen for regions (1)–(5). Here, R_{O_2} can be expressed as

$$R_{O_2} = \frac{Y_{O_2,i} - Y_{O_2,0}}{Y_{O_2,0}} \times 100\%, \tag{4.2}$$

where $Y_{O_2,i}$ denotes the mass fraction of oxygen at region (i) and $Y_{O_2,0}$ denotes the mass fraction of oxygen at the initial upstream condition. The value of $Y_{O_2,i}$ is determined by averaging the values of Y_{O_2} at three to five samples located in region (i) just behind shock waves, while the value of $Y_{O_2,0}$ is a fixed value. It is evident from figure 16 that the relative change in oxygen mass fraction for all regions is very small (less than 0.05 %), suggesting that the oxygen consumption can be ignored and consequently the flow surrounding the TW structure can be considered non-reactive. Therefore, an inert shock polar theory can be applied in the present study. Note that the pressure value of the HP region not only represents the transverse dynamics but also is an important indicator to measure the

performance of the shock polar, thus subsequent discussion focuses on the states of the HP region.

4.1. *Prediction of the high-pressure value*

To conduct shock polar calculations, one first needs to know the transverse speed D_Z, the longitudinal speed D_X of TP A and the angle χ_I, as shown in figure 15. For the purpose of usability and generality, it is necessary to establish a reasonable assumption for the basic parameters used in calculating the shock polar. This strategy allow us to theoretically derive a reasonable physical quantity for the apparent transverse dynamics of detonation.

The selection of appropriate assumptions is crucial. At the outset, we can only rely on intuitive statistical averages to hypothesize about the research object. Therefore, for the typical second kind of STW structure of single-headed detonation in a 2-D channel, several assumptions can be made as follows:

(i) Since acoustic coupling occurs between the typical second kind of STW and the acoustic wave in the induction zone of the CJ-ZND structure (see § 3.4), D_Z in equation (4.1) is assumed as a_i.

(ii) The CJ detonation is considered here (see result of figure 8), so D_X in equation (4.1) is determined as D_{CJ}.

(iii) It is assumed that the angle χ_M ranges from 90° at maximum to $90° - \alpha$ at minimum. The linear changes on space or time are considered for χ_M, thus the Mach front's average angle is $\chi_{M,avg} = (\chi_{M,min} + \chi_{M,max})/2 = 90° - 0.5\alpha$. For a 2-D single-headed detonation, since the Mach front transforms into an incident front after the STW structure collides with the wall, the angle χ_I is construed as

$$\chi_I = \chi_{M,avg} = 90° - 0.5 \arctan(a_i / D_{CJ}). \tag{4.3}$$

Based on the aforementioned assumptions, the incoming flow velocity relative to the TP A is here determined using $V_{(0)} = D_{CJ}/\cos(\alpha)$, and the angle β of incident front can be determined by $\beta = \chi_I - \alpha$. The assumed value of $\theta_{(1)}$ and other flow states behind the incident front can be obtained by substituting the assumed values of β and $V_{(0)}$ into the shock jump condition using the iterative method mentioned in Appendix C. Figure 17 displays the shock polars for the second kind of STW structure with a stoichiometric H_2/air mixture. Eventually, the pressure value and deflection angle $\theta_{(4),(5)}$ of the states (4) and (5) in the HP region of the STW can be determined by the red point in figure 17(*a*).

Moreover, the wave angle β for different shock waves in the STW can also be derived by utilizing the deflection angle $\theta_{(i)}$ of different states and the polar represented in figure 17(*b*). These parameters enable us to construct a shock wave pattern that closely resembles the shock wave system of STW structure, as shown in figure 15. The extended segments on the blue and green polar are depicted in figure 17, illustrating the potential state behind the secondary Mach stem and the secondary reflection shock wave. On the one hand, for a Mach reflection in free space, the Mach stem can either increase (extended segment on blue polar) or decrease the deflection angle, e.g. the overall Mach reflection of asymmetric shock waves (Ben-Dor 2007). On the other hand, for the secondary reflection shock wave, a shock system that is similar to the von Neumann reflection is considered, which means the states (4) and (5) in some situations can be given by the intersection point between the blue polar and the extended segment of the green polar. One can note that this paper stipulates that the Mach stems (M and line segment BD in figure 15) only exist when the solution corresponds to a strong shock wave.

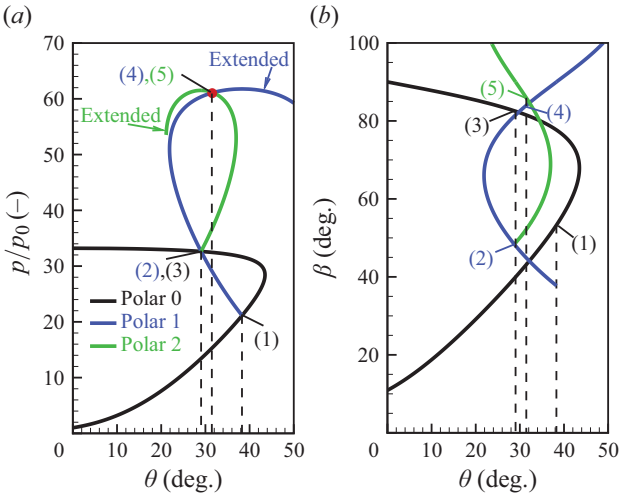

Figure 17. The polars of (*a*) pressure ratio and (*b*) wave angle with a stoichiometric H_2/air mixture. The numbers in parentheses represent the flow states and wave angles in the corresponding flow regions. The extended segments are the strong shock part of the shock polar with a wave angle larger than 90°.

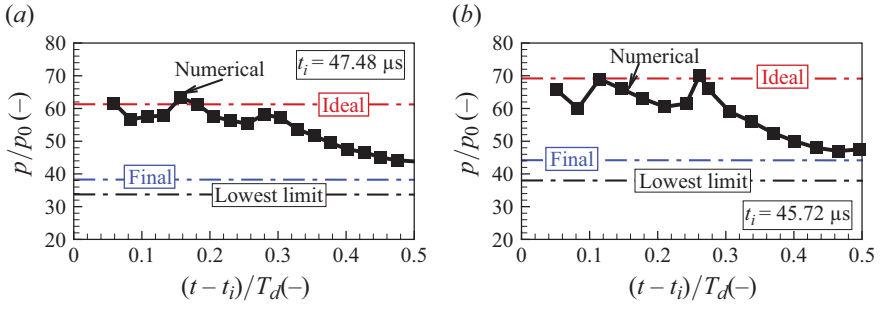

Figure 18. The pressure ratio given by the shock polar and numerical result with (*a*) stoichiometric H_2/air and (*b*) stoichiometric H_2/O_2 mixtures. Dashed-dotted lines represent the values determined by shock polar. Ideal value: the value calculated based on assumptions in this sub-section, final and lowest limit values: the values calculated based on the evolution behaviour of the STW structure discussed in the next sub-section.

To verify the accuracy of the prediction of polar presented in this paper, figure 18 displays the pressure ratio p/p_0 changes over time in the HP region of the second kind of STW structure for both mixture cases, by using numerical simulation and shock polar. At each moment, the HP value for the numerical simulations is determined by averaging the numerical values from three to five grids. These grids are positioned approximately two grid points downstream of point B and its adjacent shock waves. Here, the given time range for figure 18 corresponds to the stage at which the TW propagates upward from the lower wall to the upper wall for both mixtures, as shown in figure 13. It can be observed from figure 18 that, in the early phases, the pressure values from the numerical results align well with the ideal value, indicating the effectiveness of the theoretical method in this paper and the reasonability of the assumptions made above.

Since the assumptions for the polar do not account for the temporal dynamics of the second kind of STW structure, the ideal values (indicated by the red dash-dot lines in figure 18), determined by the shock polar based on the assumptions in this section, remain

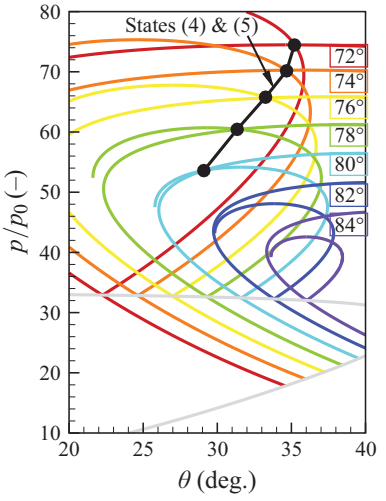

Figure 19. The $(p/p_0, \theta)$ polars at different χ_I with a stoichiometric H_2/air mixture.

constant over time. However, the numerical data indicate that the pressure in the HP region does not remain steady but decays over time. When the STW approaches the wall, there is a substantial discrepancy between the ideal values and the numerical results. This difference is analysed in the following sub-subsection.

4.2. *Transverse dynamic behaviours*

To explore the impact of time-dependent behaviours of the STW structure on the pressure values of states (4) and (5), several key influencing factors are sought here through the shock polar method combined with the numerical results of the 2-D detonation described in previous sections. Firstly, one notes that angle χ_I can continuously increases to 90° by observing figure 13. However, the influence of the change of χ_I on the flow states around STW is still unclear.

To understand the influence of the angle χ_I on the HP value of states (4) and (5), figure 19 presents a set of $(p/p_0, \theta)$ polar as the angle χ_I varies, while the track angle α of TP A is still determined by the assumptions in § 4.1. The results show that, as χ_I changes, the predicted pressure values of the states (4) and (5) form a trajectory marked in the black curve in figure 19. The evolution of the pressure value along this curve suggests that an increase in the incident front angle χ_I leads to a decrease in the pressure value of states (4) and (5), which is due to a reduction in the total flow Mach number of state (1). This pressure change coincides precisely with the described pressure decay characteristics in figure 18, thus the angle χ_I is considered as a key factor influencing the pressure of states (4) and (5). Interestingly, as shown in figure 19, when χ_I is 82° or 84°, the states (4) and (5) cannot be given by the polar, which means the von Neumann criterion (Ben-Dor 2007; Peng *et al.* 2019) is not reached, indicating that the flow intensity of state (1) cannot form a secondary Mach reflection for larger χ_I. However, the numerical results of wave structures in figure 13 suggest that, even when χ_I tends very close to 90°, the TW still manifests as an STW structure, implying that the states (4) and (5) may simultaneously depend on other controlling factors besides χ_I.

Recall that, in assumption (ii) of § 4.1, the longitudinal speed D_X is set to a constant value (D_{CJ}). Actually, before TP A contacts the wall, D_X should be close to the incident front speed D due to the incident front being nearly perpendicular to the wall, as shown by

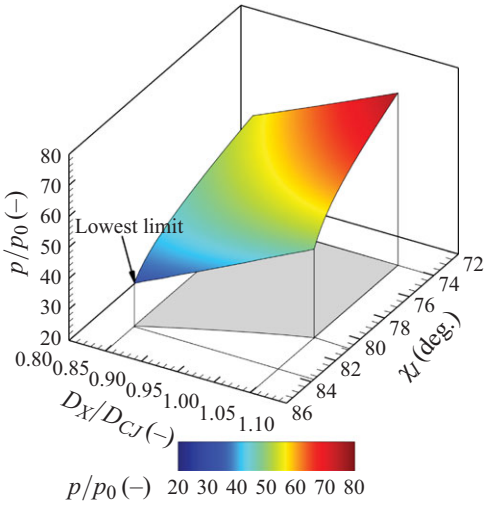

Figure 20. Dimensionless pressure of states (4) and (5) as a function of the angle χ_I and the longitudinal speed D_X of TP A with a stoichiometric H_2/air mixture and $D_Z = a_i$.

the wave structure of $t = 48.40$ μs in figure 13(a) and $t = 46.40$ μs in figure 13(b). When TP A is about to interact with the wall dd', D_X equals D and is less than D_{CJ}, and the transient deviation between D_X and D_{CJ} can reach up to 20%, as indicated by figure 8. Thus, the assumption that $D_X = D_{CJ}$ may lead to a discrepancy between the predicted values and actual ones.

To explore the influence of D_X on the pressure of states (4) and (5) in the HP region, D_Z is fixed as a_i, and the pressure changes for states (4) and (5) under different χ_I and D_X are depicted in figure 20. The decrease in D_X leads to an overall weakening of the STW structure, resulting in a reduction in the pressure values of states (4) and (5), as shown in figure 20. Therefore, D_X can also be considered a key factor for the decay of pressure in the HP region. Furthermore, with the longitudinal speed D_X decrease, the upper limit of incident front angles has increased from 81° at $D_X = D_{CJ}$ to 84° at $D_X = 0.85D_{CJ}$, and the range of incident front angles has expanded, as demonstrated by figure 20. This expansion is attributed to the decreased incoming flow Mach number in the ξ-direction (the decreased incident front strength), which indirectly results in the elevated transverse (η-direction) flow Mach number downstream of the incident front. Eventually, this adjustment provides ample flow intensity in region (1), facilitating the formation of secondary Mach reflection.

On the other hand, combining the results of the present and previous works (Radulescu *et al.* 2007; Liang *et al.* 2007; Frederick *et al.* 2023), it can be concluded that there exists a minimum D_X for the self-sustained 2-D detonation, which is approximately $0.85D_{CJ}$ for the typical second kind of STW structure as shown in figure 8(a,d) in the present study. Although the reduction in D_X broadens the range of χ_I, as shown in figure 20, the upper limit of χ_I always remains well below 90 degrees, indicating that there are still other parameters controlling the TW structure and flow state. It is observed in figure 12 that the transverse speed D_Z of TP A exceeds a_i for a long time, but D_Z is assumed as the sound speed a_i in the induction zone of the CJ-ZND structure. For this reason, the focus now shifts to the effects of the potential last parameter, D_Z.

Figure 21 depicts the variation of pressure with respect to χ_I and D_Z, where D_X is maintained at the minimum value $0.85D_{CJ}$. Indeed, the increase in D_Z leads to a rise in

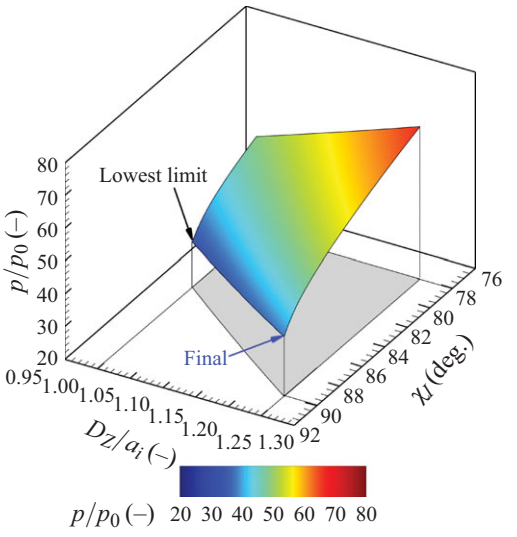

Figure 21. Dimensionless pressure of states (4) and (5) as a function of the angle χ_I and the transverse speed D_Z of TP A with a stoichiometric H_2/air mixture and $D_X = 0.85D_{CJ}$.

the pressure value of the HP region, which is attributed to the strengthening of the entire STW structure during the increase in the transverse speed. Increasing the transverse speed at the TP directly raises the transverse flow Mach number in region (1) relative to point A. This facilitates adequate flow intensity for forming a secondary Mach reflection structure. Therefore, even when χ_I equals 90 degrees, the TW structure remains a strong type.

In summary, two key factors dominate the pressure decay in the HP region: the incident front angle χ_I and the speed D_X. Under the influence of both factors, there is a theoretical lowest limit for the pressure value of the states (4) and (5), as indicated by the black arrows in figures 20 and 21. This lowest limit is also marked in figure 18. On the other hand, the variations in the third factor, i.e. the transverse speed D_Z, cause an increase in the HP value of states (4) and (5). Since χ_I, D_X, and D_Z change concurrently, the pressure values derived from numerical simulations are disabled to reach this theoretical minimum. For the single-headed detonation investigated in the present study, due to theTW structure needing to remain an STW structure throughout, there exists a minimum value for the upper limit of D_Z. This ensures that, even when χ_I is 90° and D_X is $0.85D_{CJ}$, the HP region persists. As depicted in figure 21, the dynamic change of the factors ultimately settles at the position (indicated by the blue arrow) where χ_I equals 90 degrees, indicating the minimum value (approximately $1.25a_i$) for the upper limit of D_Z and the pressure value of the HP region at the final situation. This final value is also plotted in figure 18 for comparison. It is evident that the three specific values obtained by shock polar effectively capture the features of the transverse structure dynamics.

Simultaneously, combining the discussions in this sub-section with those in §§ 3.3 and 3.4, it is evident that increasing the channel width results in a higher transverse speed of the TW structure, but has little effect on the longitudinal speed of the TP (with an average value of D_{CJ} and a minimum value in the range of 0.80–$0.85D_{CJ}$, as shown in figures 8 and 10) and the angle of the incident front (the angle tends towards 90°, see figures 11 and 13). As a result, the increase in channel width primarily enhances the transverse strength of the STW structure. A wider channel induces stronger collisions between the STW and the wall, which facilitates the formation of new TPs and leads to the

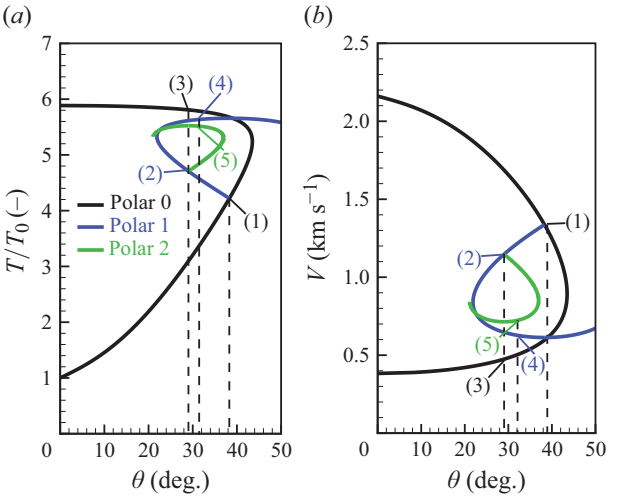

Figure 22. The polars of (*a*) temperature ratio and (*b*) flow velocity with a stoichiometric H_2/air mixture. The numbers in parentheses represent the flow states in the corresponding flow regions.

failure of the MLE. Conversely, a narrower tube prevents the STW structure from meeting the minimum upper limit condition of the transverse speed, causing the STW structure to be unsustainable and leading to the failure of the MLE as well.

4.3. *Quantitative identification on strong transverse wave*

In the discussion of the § 3.4, the classification of STW structures is primarily based on observation, which is somewhat subjective and qualitative. Therefore, identifying the quantitative difference between the two typical kinds of STW structures is of primary significance. The constant-volume combustion (CVC) theory is widely used for the calculation of ignition times in shock-induced combustion, such as predicting the induction zone length in oblique detonations (Zhang *et al.* 2019*b*) and the strong ignition time (Huang *et al.* 2022). To quantitatively identify the structure of the STW, the reaction spatial scale calculations downstream of TP B based on CVC theory are performed in this section.

For spatial-coordinate-based CVC computation, a determination of the temperature and total flow velocity conditions near the STW is necessary. As a result, figure 22 displays the temperature ratio and total flow velocity polars based on the shock polar method described in § 4.1. By integrating the pressure and temperature polars (see figures 17*a* and 22*a*, respectively), and assuming that the mixture in region (4) near point B remains as an unburned mixture, the variation of temperature with combustion time τ_{CVC} can be determined using CVC theory. To characterize the spatial scale of the reaction zone near the STW, we define a transverse chemical reaction distance $\zeta_r = \tau_{CVC} V_{(4)}$, where $V_{(4)}$ is the total flow velocity of state (4), as shown in figure 22(*b*).

Figure 23 shows the variation of dimensionless temperature T/T_0 with respect to dimensionless transverse reaction distance ζ_r/Δ_{ind} (Δ_{ind} is the induction length from the 1-D CJ-ZND structure) for the typical second kind of STW with the stoichiometric H_2/air and H_2/O_2 mixtures of the current study. For the purpose of comparison, the temperature profiles of the typical first kind of STW with a stoichiometric H_2/air mixture observed in Tsuboi & Hayashi (2007) and stoichiometric H_2/O_2 mixture observed in Tsuboi, Hayashi & Koshi (2009) are also calculated. For several CVC cases shown in figure 23, the initial parameters required for shock polar calculation used in CVC computations are listed in

Work	Mixture	D_X (m s^{-1})	D_Z (m s^{-1})	χ_I (°)	α (°)	p_0 (kPa)	T_0 (K)
Present	H_2/air(stoich.)	1966	895	77.75	24.5	60	300
Present	H_2/O_2(stoich.)	2751	1240	77.85	24.3	20	300
Tsuboi & Hayashi (2007)	H_2/air(stoich.)	1980	1980	80.00	45.0	100	300
Tsuboi *et al.* (2009)	H_2/O_2(stoich.)	2802	2706	79.00	44.0	50	300

Table 2. Calculation parameters of shock polar serving CVC computations.

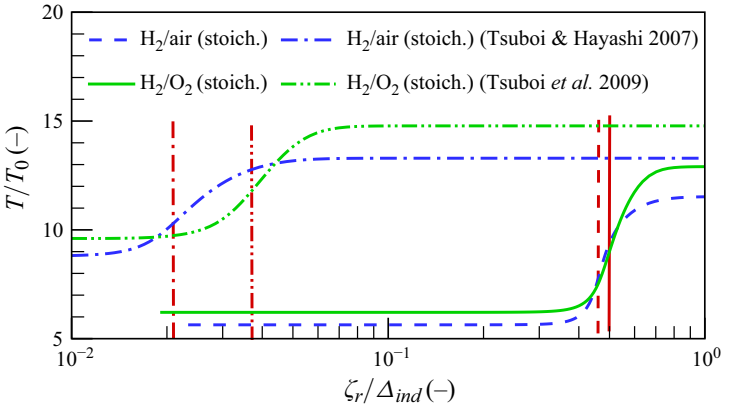

Figure 23. Dimensionless temperature as a function of the dimensionless transverse chemical reaction distance with constant-volume combustion and the parameters of state (4). The red lines indicate the locations of ignition.

table 2. Among them, the initial parameters for the second kind of STW structure are given by the assumptions in § 4.1, while the initial parameters for the first kind of STW structure are derived from measurements of previous research (Tsuboi & Hayashi 2007; Tsuboi *et al.* 2009).

Based on figure 23, we can define an ignition delay distance ζ_i as the distance from the start of the reaction (i.e. TP B) to the location of ignition and this is used to derive a quantitative index of reactivity. The values of ζ_i/Δ_{ind} for different cases are indicated by the red lines in figure 23, where a rapid increase in temperature is observed. Obviously, due to the extremely short ignition delay distance ζ_i ($\zeta_i/\Delta_{ind} \ll 1$, indicated by red dash-dot and red dash-dot-dot lines in figure 23) downstream of TP B in the STW structure of Tsuboi & Hayashi (2007) and Tsuboi *et al.* (2009), a TD is observed, rendering the entire STW structure of spinning detonation as the typical first kind of STW structure. On the contrary, a quite long ignition delay distance ($\zeta_i/\Delta_{ind} \to 1$) is required downstream of TP B of the TW structure in the present detonation, suggesting the presence of an unreacted groove containing premixed mixture. This characteristic is a typical feature of the second kind of STW structure described in this paper.

There is an order of magnitude difference in reactivity (i.e. ignition delay distance) between the typical two kinds of STW structures. The downstream ignition delay distance at the TP B of the typical second kind of STW structure is comparable to the induction zone length, which shows consistency with the results shown in figure 14. This further validates the assumptions proposed in § 4.1. Interestingly, as shown in table 2, the track angle of the typical first kind of STW structure always approaches 45°, whereas the track

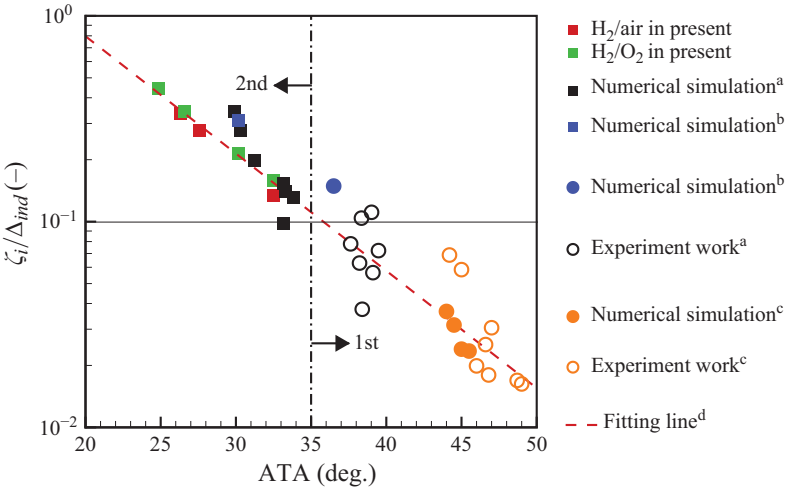

Figure 24. Relationship between the ATA and the ζ_i/Δ_{ind} under different conditions. The square and circular markers represent the propagation of detonation waves in rectangular and circular channels, respectively. The black dash-dot line represents the median of the ATA for the two typical kinds of STW structures. [a]Meagher *et al.* (2023), [b]Crane *et al.* (2023), [c]Tsuboi *et al.* (2009) and [d] $\log(\zeta_i/\Delta_{ind}) = 1.041 - 0.057\overline{\alpha}$.

angle of the typical second kind of STW structure is closer to 24°. Here, the track angle actually corresponds to the average track angle of the TP. This indicates an important parameter for distinguishing the kinds of STW structures in detonations, namely, by measuring the average track angle (ATA, calculated by $\overline{\alpha} = \arctan(\lambda/\ell)$, where λ and ℓ are the width and length of cell, respectively) of the TPs on the cell structure to assess the reactivity of the TW structure.

In § 3, the classification of STW structures is somewhat arbitrary, as all STW structures discussed are classified as the second kind, which is somewhat subjective. To provide a quantitative criterion for distinguishing both kinds of the STW structures for the purpose of engineering or experiments, figure 24 further illustrates the relationship between the ATA and ζ_i/Δ_{ind} under different conditions, in which the angle χ_I follows equation (4.3) for obtaining relevant shock polars. One can observe that the ATAs of detonation in the rectangular channel are smaller than the value of a median (as shown by the vertical dash-dot line in figure 24), and Austin (2003) also pointed out that the ATA in a rectangular channel is 33° and is less than the median. Whereas the ATAs in the circular channel are all greater than the value of median. Therefore, this median is important for distinguishing or identifying the characteristics of confined spaces where TWs are located.

On the other hand, a logarithmic law between the ATA and the dimensionless ignition delay distance was observed after conducting a linear regression analysis (as indicated by the red dashed line in figure 24) for all of the data appearing in figure 24. Notably, the value of the point where the red dashed line intersects the horizontal line at $\zeta_i/\Delta_{ind} = 0.1$ is found to be very close to the median. Thus, this median, $\overline{\alpha} = 35°$, that corresponds to $\zeta_i/\Delta_{ind} = 0.1$, is crucial as it reflects both the characteristics of the confined space and the reaction scale. Furthermore, given the ease of obtaining the ATA and its ability to represent the kinematic characteristics of STW structures, the distinction and classification of STW structures are ultimately realized by determining the value of the ATA. If the angle is greater than the median, the STW structure is classified as first kind; otherwise, it is classified as second kind.

As previously mentioned, the detonation in circular channels exhibits a significantly different TW structure (often characterized by the first kind of STW structure), which is due to the more complex interactions between the TWs and the circular channel walls, reflecting complex 3-D effects. This paper primarily focuses on 2-D detonations and cannot fully explain this phenomenon. Moreover, the detonations discussed in this study propagate in weakly unstable and moderately unstable mixtures. For highly unstable mixtures, complex interactions between shock waves and turbulence may occur within the detonation wave, and the applicability of the current theory requires further consideration. Accordingly, these two aspects will need to be addressed in future work.

5. Concluding remarks

Utilizing the reactive Euler equations with detailed reactions, the detonations near the critical propagation state are investigated in 2-D channels of different widths filled with the stoichiometric undiluted and nitrogen-diluted H_2/O_2 mixtures. As the channel width varies, the detonation wave exhibits several propagation modes, including pulsed mode, single-headed mode, single-dual-headed critical mode and dual-headed mode. When detonation propagates in a pulsed mode, the TW structure within the detonation wave appears intermittently. The MLE in the channel occurs in the single-headed mode regime. The varying sensitivity of premixed mixtures to temperature affects the extent of the single-headed mode region and also changes how the MLE fails. For the relatively stable stoichiometric H_2/O_2 mixture, the failure of the MLE is primarily caused by the Mach reflection bifurcation, in which the jet causes deformation of the Mach front. While for a stoichiometric H_2/air mixture, the failure of the detonation MLE is controlled by a novel mechanism, in which the interaction of explosion waves originating from the unreacted pocket behind the detonation front with the front leads to a bifurcation of the front and the failure of MLE.

Numerical results suggest that all TWs under the studied cases can be featured as STWs, indicating the importance of STWs. Most of the STW structure is the second kind defined in the current study. Under the conditions near the threshold of the critical propagation state, the average transverse speed of the STW approaches the sound speed of the induction zone of the CJ-ZND structure, which means that an acoustic coupling occurs between the typical second kind of STW and the acoustic wave in the induction zone. The decrease in channel width leads to the STW structure not being able to exist persistently, resulting in the disappearance of the detonation front's TP. This shows another mechanism that renders the MLE ineffective. Essentially, channel width variations affect the entire TW structures' strength and period, resulting in MLE failure.

The pressure value of the HP region around the STW structure is predicted by the shock polar method, given the transverse speed D_Z and longitudinal speed D_X of TP A and the incident front angle χ_I. The predicted values agree well with numerical results for the second kinds of STW structures for both mixtures. A transverse dynamic behaviour of the STW is exhibited in terms of the time-dependent variation of the pressure of the HP region within the STW structure. The parameters that impact the flow states and wave structure, namely, χ_I, D_X and D_Z, are identified through shock polar analysis. During the propagation of the TW, an increase in the incident front angle and a decrease in the longitudinal speed cause a pressure decay of the HP region, while an increase in the transverse speed leads to a pressure rise. To maintain an STW structure in detonations, there exists a minimum value for the upper limit of the transverse speed. From numerical results, it is observed that these parameters have several limiting values, and the pressure

value in the HP region derived from these values can effectively describe the transverse dynamic characteristics.

Downstream of TP B, the dimensionless ignition delay distance calculated using the CVC theory adequately identifies the reactivity or kind of STW structure. The ignition delay distance of the typical first kind of STW structure is much smaller than the induction zone length of the 1-D CJ-ZND structure, while the ignition delay distance of the typical second kind of STW structure is comparable to this induction zone length. Note the track angle of TP A fundamentally demonstrates the kinematic characteristics of the STW structure. By measuring the ATA of the TPs on the cell structure, the kind of the STW structure can be assessed from a geometrical kinematics perspective.

In fact, the methods advanced in this paper can efficiently and conveniently obtain design criteria to serve engineering applications. Additionally, the theory constructed in this paper does not involve any channel geometric information, therefore, it can be applied to the TW study of other types of detonation, such as cylindrical detonations (Jia *et al.* 2023) and curved detonations (Yan *et al.* 2024), in the future.

Acknowledgements. We thank the anonymous reviewers for their comments/suggestions which helped to improve this paper.

Funding. The work was supported by the National Natural Science Foundation of China (No. 12472335).

Declaration of interests. The authors report no conflict of interest.

Appendix A. Chemical reaction mechanism

The chemical reaction mechanism and corresponding parameters for hydrogen combustion are shown in table 3.

Appendix B. Convergence test of grid resolution

In the present numerical simulations of 2-D gaseous detonation, a multi-level grid strategy for adaptive division of the computational domain is used. Meanwhile, the density gradient of the flow field is used as the criterion for grid refinement. To determine the required grid size, we designate the length of the chemical induction zone Δ_{ind} as the distance from the von Neumann pressure front to the peak of the heat release rate in the CJ-ZND structure of the detonation wave. Table 4 presents the 2-D grid resolution parameters under three grid sizes. Here, N represents the number of grids within a Δ_{ind}, where N_{coarse} is the resolution parameter of grids in the coarsest region and N_{fine} denotes the resolution parameter in the finest region. A grid convergence study is conducted based on the grid resolutions listed in table 4.

Whereas the detonation of the stoichiometric H_2/air mixture shown in table 1 exhibits higher temperature sensitivity, it is also more sensitive to the grid resolution. Consequently, this mixture is used to conduct the grid resolution test. The grid resolution test is performed in a 2-D straight channel, as shown in figure 2. Figure 25 displays the recorded numerical foils of HP under three cases, with the channel width equal to 1 mm. As can be seen from figure 25, the flow fields recorded for all three grid resolution cases have approached nearly steady periodic propagation of the detonations. Notably, when the grid resolution is lower, as in figure 25(a), the area of the HP region is slightly larger than that in figure 25(b,c), indicating that the grid resolution of case I is insufficient. Comparing figure 25(b,c), their exhibited HP features are almost identical, making it difficult to discern any differences from the numerical foils, which means that the flow field using the grid resolution of case II is converged.

			A	n	E_a
(1)	$H + O_2 = O + OH$		$1.04E+14$	0.00	$1.531E+04$
(2)	$O + H_2 = H + OH$	Duplicate	$3.82E+12$	0.00	$7.948E+03$
		Duplicate	$8.79E+14$	0.00	$1.917E+04$
(3)	$H_2 + OH = H_2O + H$		$2.16E+08$	1.51	$3.430E+03$
(4)	$OH + OH = O + H_2O$		$3.34E+04$	2.42	$-1.930E+03$
(5)	$H_2 + M = H + H + M$		$4.58E+19$	−1.40	$1.040E+05$
	$\varepsilon(H_2) = 2.5$, $\varepsilon(H_2O) = 12.0$				
(6)	$O + O + M = O_2 + M$		$6.16E+15$	−0.50	$0.000E+00$
	$\varepsilon(H_2) = 2.5$, $\varepsilon(H_2O) = 12.0$				
(7)	$O + H + M = OH + M$		$4.71E+18$	−1.00	$0.000E+00$
	$\varepsilon(H_2) = 2.5$, $\varepsilon(H_2O) = 12.0$				
(8)	$H_2O + M = H + OH + M$		$6.06E+27$	−3.32	$1.208E+05$
	$\varepsilon(H_2) = 3.0$, $\varepsilon(H_2O) = 0.0$, $\varepsilon(O_2) = 1.5$, $\varepsilon(N_2) = 2.0$				
	$H_2O + H_2O = H + OH + H_2O$		$1.01E+26$	−2.44	$1.202E+05$
(9)	$H + O_2 (+M) = HO_2 (+M)$	k_∞	$4.65E+12$	0.44	$0.000E+00$
		k_0	$6.37E+20$	−1.72	$5.250E+02$
	$F_c = 0.5$, $T^{***} = 1.0E{-}30$, $T^* = 1.0E+30$				
	$\varepsilon(H_2) = 3.0$, $\varepsilon(H_2O) = 21.0$, $\varepsilon(O_2) = 1.1$, $\varepsilon(N_2) = 1.5$				
(10)	$HO_2 + H = H_2 + O_2$		$2.75E+06$	2.09	$-1.451E+03$
(11)	$HO_2 + H = OH + OH$		$7.08E+13$	0.00	$2.950E+02$
(12)	$HO_2 + O = O_2 + OH$		$2.85E+10$	1.00	$-7.239E+02$
(13)	$HO_2 + OH = H_2O + O_2$		$2.89E+13$	0.00	$-4.970E+02$
(14)	$HO_2 + HO_2 = H_2O_2 + O_2$	Duplicate	$4.20E+14$	0.00	$1.200E+04$
		Duplicate	$1.30E+11$	0.00	$-1.630E+03$
(15)	$H_2O_2 (+M) = OH + OH (+M)$	k_∞	$2.00E+12$	0.90	$4.875E+04$
		k_0	$2.49E+24$	−2.30	$4.875E+04$
	$F_c = 0.42$, $T^{***} = 1.0E{-}30$, $T^* = 1.0E+30$				
	$\varepsilon(H_2) = 3.7$, $\varepsilon(H_2O) = 7.5$, $\varepsilon(O_2) = 1.2$, $\varepsilon(N_2) = 1.5$, $\varepsilon(H_2O_2) = 7.7$				
(16)	$H_2O_2 + H = H_2O + OH$		$2.41E+13$	0.00	$3.970E+03$
(17)	$H_2O_2 + H = HO_2 + H_2$		$4.82E+13$	0.00	$7.950E+03$
(18)	$H_2O_2 + O = HO_2 + OH$		$9.55E+06$	2.00	$3.970E+03$
(19)	$H_2O_2 + OH = HO_2 + H_2O$	Duplicate	$1.74E+12$	0.00	$3.180E+02$
		Duplicate	$7.59E+13$	0.00	$7.270E+03$

Table 3. Hydrogen combustion model. Units are cm^3 mol s cal K; $k = AT^n \exp(-E_a/RT)$.

Case no.	Case I	Case II	Case III
$N_{coarse}(1/\Delta_{ind})$	17	13	17
$N_{fine}(1/\Delta_{ind})$	68	104	136

Table 4. Grid resolution parameters.

Furthermore, the pressure value changes along the centrelines (e.g. dash-dot line in figure 25*b*) of the three numerical foils of HP are plotted in figure 26 for a quantitative comparison. Since the intensity of the detonation wave decreases with an increase of grid resolution (Mazaheri, Mahmoudi & Radulescu 2012), it can be seen that the pressure peak of the curve under the grid resolution of case I is significantly larger than the pressure peaks of the other two curves, while the difference between pressure peaks of cases II and III can be almost neglected. In addition, the gaps of pressure fluctuations on the curves of cases II and III in figure 26 are equal to 2.040 mm and 2.041 mm, respectively, and are very

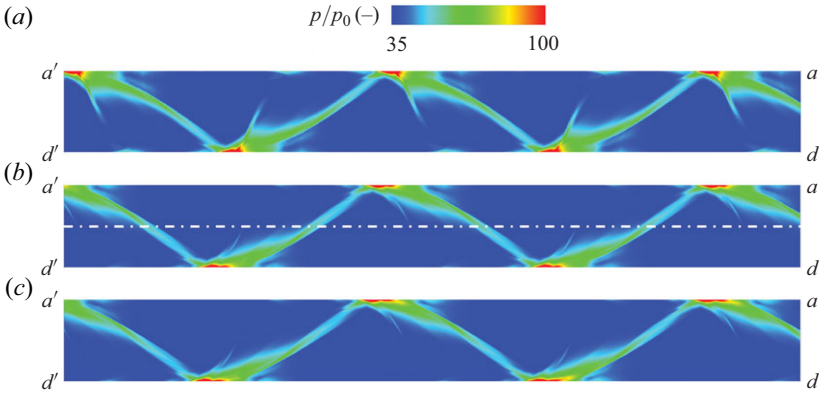

Figure 25. Numerical foils of HP for stoichiometric H_2/air detonations using the grid resolution of (*a*) case I, (*b*) case II and (*c*) case III in a 2-D domain of channel with $W = 1$ mm.

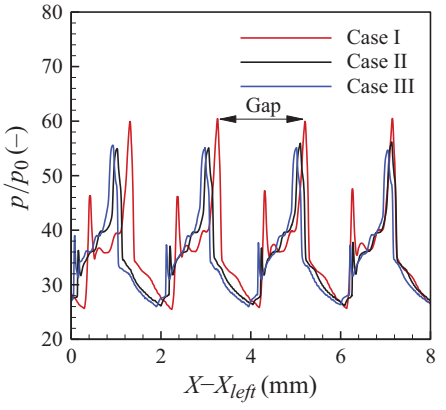

Figure 26. Distributions of pressure along the centreline of the numerical foil of HP for stoichiometric H_2/air detonations using the grid resolution of different cases in 2-D domain of the channel with $W = 1$ mm. Here, X represents the axial distance (direction of detonation propagation) in the laboratory frame, and X_{left} is located on edge $a'd'$ in figure 25.

close to each other, which means that there is convergence, that is, the flow characteristics are relatively independent of the grid resolution.

The grid resolution of case II is already sufficient for detonation simulations near a channel width of 1 mm. To ensure the grid resolution is suitable for more complex detonation scenarios, new grid resolution convergence tests were conducted for detonations in channels with wider widths. Figure 27 shows the numerical foils of HP for the detonation of a stoichiometric H_2/air mixture in a channel with width of 3.5 mm under the grid resolution conditions shown in table 4. Clearly, the numerical foil of HP for case I (figure 27*a*) is completely different from that for case II and case III (figure 27*b*,*c*). For the low-resolution case in figure 27(*a*), there is only one HP stripe, which is due to pseudo-detonation (a non-physical phenomenon that occurs under low-resolution conditions) in the flow field. Therefore, this grid resolution parameter is unacceptable. However, figure 27(*b*,*c*) exhibits morphological similarity in the numerical foil of HP, including the half-cell and one-cell patterns and the transition from the single-headed to the dual-headed mode. It should be noted that, due to the instability and tendency

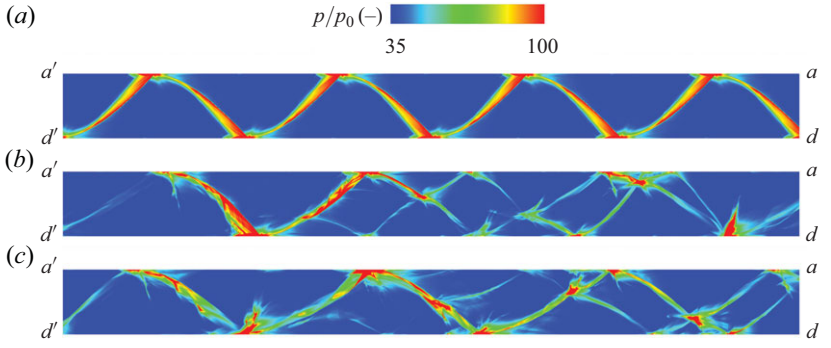

Figure 27. Numerical foils of HP for stoichiometric H_2/air detonations using the grid resolution of (*a*) case I, (*b*) case II and (*c*) case III in 2-D domain of the channel with $W = 3.5$ mm.

to display chaotic characteristics of the detonation for the stoichiometric H_2/air mixture (Daimon & Matsuo 2007), it is difficult for the numerical foil images (see figure 27*b*,*c*) to be completely consistent, and the convergence of quantitative analysis is challenging to achieve. Accordingly, results in figure 27 mean that both sets of grid resolution parameters for case II and case III once again satisfy grid convergence for more complex detonation circumstance.

Basically, the grid resolutions of cases II and III fall within the range recommended by Sharpe (2001), who stated that the grid resolution for 2-D detonation numerical simulations needs to be greater than $50/\Delta_{ind}$ to describe the multi-dimensional characteristics of detonation waves. In summary, given that the computations using the grid parameters of case II sufficiently capture the complex flow field features with relatively low computational cost, the grid parameters of case II are used for grid generation in all computations throughout this paper.

Appendix C. Shock polar method

For a system with a calorically perfect gas, shock jump conditions can be summarized into simple formulas, thus directly solving the post-shock flow state. However, because multi-species thermodynamics is used in this paper, such simple formulas to solve for changes in the flow state do not exist in reality. Therefore, an iteration method derived from reference (Browne *et al.* 2023) is adopted to solve the shock jump conditions, and the specific iterative process is as follows:

(i) Given known variables, i.e. the physical quantities of upstream state 0, such as, w_0, p_0, v_0, $Y_{10}, \cdots, Y_{N0}$, where w is the flow velocity normal to the shock wave, p is the pressure of the fluid, v is the specific volume of the fluid and Y_k is the mass fraction of the kth species. Set tolerance $\varepsilon = 1 \times 10^{-4}$;

(ii) the ratio of specific volumes between the upstream and downstream (i.e. state 1) is defined as $\Gamma = v_1/v_0$. It is assumed that $\Gamma_{min} < \Gamma < \Gamma_{max}$. Typically, $\Gamma_{min} = 1/5$, $\Gamma_{max} = 1/1.005$;

(iii) at the beginning of the iteration, set Γ to Γ_{min}. Otherwise, $\Gamma = (v_1^* + \Delta v)/v_0$, where the superscript $*$ indicates that the value of this physical quantity is tentative. Calculate the tentative value p_1^* of downstream pressure using the momentum jump equation

$$p_1^* = p_0 + w_0^2(1 - \Gamma)/v_0; \tag{C1}$$

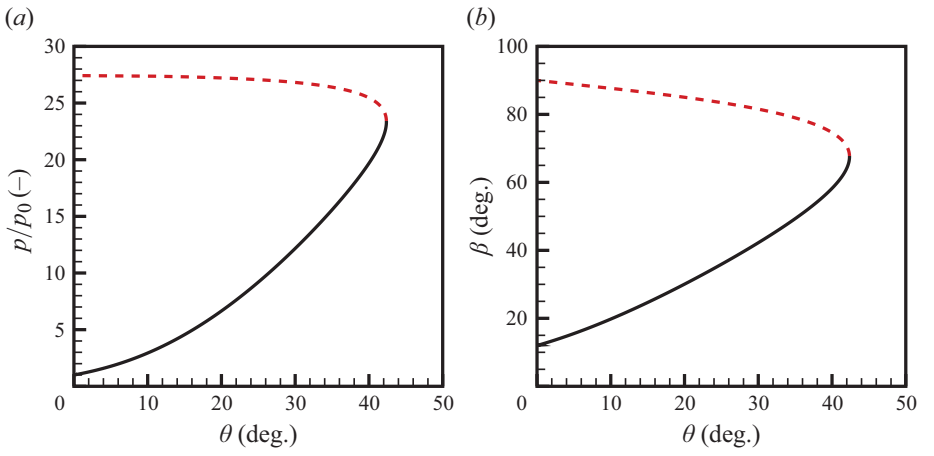

Figure 28. The polars of (*a*) pressure ratio and (*b*) wave angle with CJ speed of the stoichiometric H_2/air mixture in table 1. The dashed and solid lines indicate the strong and weak shock waves, respectively.

(iv) solve the specific enthalpy of the mixture behind the wave using the equation of state, i.e.

$$v_1^* = \Gamma v_0, \tag{C2}$$

$$h_1^* = h(p_1^*, v_1^*, Y_{11}, \cdots, Y_{N1}); \tag{C3}$$

(v) calculate the enthalpy using the energy jump equation

$$h_1 = h_0 + w_0^2(1 - \Gamma^2)/2; \tag{C4}$$

(vi) evaluate the difference between two enthalpies obtained from equations (C3) and (C4)

$$r = (h_1 - h_1^*); \tag{C5}$$

(vii) if $|r| \leq \varepsilon$, return final post-shock state 1. Else, let $\Delta v = \delta$ (δ is usually 1×10^{-4}), use steps iii–vi to obtain an $r^{\#}$, and determine the appropriate Δv using the Newton method, which is expressed as

$$\Delta v = \frac{-r\delta}{r^{\#} - r}, \tag{C6}$$

iterate steps iii–vii until $|r| \leq \varepsilon$.

When a shock wave forms an angle β with the incoming flow, it compresses the fluid, causing a deflection angle θ between the post-shock and pre-shock flow. By adjusting β (i.e. $w_0 = V \sin(\beta)$, where V is the total incoming flow velocity), a range of different post-shock flow states can be given using shock jump conditions. This routine allows us to draw curves made up of different variables. If a curve in a graph shows the relationship between the deflection angle θ and another physical quantity, then the curve is termed a shock polar. Figure 28 presents the shock polars of pressure ratio and wave angle for incoming flow velocity at the theoretical CJ detonation speed of the stoichiometric H_2/air mixture in table 1.

References

Austin, J.M. 2003 The role of instability in gaseous detonation. *PhD thesis*, California Institute of Technology.

Austin, J.M., Pintgen, F. & Shepherd, J.E. 2005 Reaction zones in highly unstable detonations. *Proc. Combust. Inst.* **30** (2), 1849–1857.

Ben-Dor, G. 2007 *Shock Wave Reflection Phenomena*. Springer.

Boulal, S., Vidal, P., Zitoun, R., Matsumoto, T. & Matsuo, A. 2018 Experimental investigation on detonation dynamics through a reactivity sink. *Combust. Flame* **196**, 11–25.

Browne, S.T., Ziegler, J.L., Bitter, N.P., Schmidt, B.E., Lawson, J. & Shepherd, J.E. 2023 Sdtoolbox: numerical solution methods for shock and detonation jump conditions. *Tech. Rep.* FM2018.001. Explosion Dynamics Laboratory, Graduate Aerospace Labortories, California Institute of Technology.

Burke, M.P., Chaos, M., Ju, Y., Dryer, F.L. & Klippenstein, S.J. 2012 Comprehensive H_2/O_2 kinetic model for high-pressure combustion. *Intl J. Chem. Kinet.* **44**, 444–474.

Cai, X., Xu, F., Deiterding, R., Chen, W. & Liang, J. 2023 Effects of activation energy on irregular detonation structures in supersonic flow. *Phys. Fluids* **35** (12), 125110.

Chase, M.W., Curnutt, J.L., Prophet, H., McDonald, R.A. & Syverud, A.N. 1975 JANAF thermochemical tables, 1975 supplement. *J. Phys. Chem. Ref. Data* **4** (1), 1–176.

Chinnayya, A., Hadjadj, A. & Ngomo, D. 2013 Computational study of detonation wave propagation in narrow channels. *Phys. Fluids* **25** (3), 036101.

Crane, J., Lipkowicz, J.T., Shi, X., Wlokas, I., Kempf, A.M. & Wang, H. 2023 Three-dimensional detonation structure and its response to confinement. *Proc. Combust. Inst.* **39** (3), 2915–2923.

Daimon, Y. & Matsuo, A. 2007 Unsteady features on one-dimensional hydrogen-air detonations. *Phys. Fluids* **19**, 112–122.

Edwards, D., Parry, D. & Jones, A.T. 1966 The structure of the wave front in spinning detonation. *J. Fluid Mech.* **26**, 321–336.

Fay, J.A. 1952 A mechanical theory of spinning detonation. *J. Chem. Phys.* **20**, 942–950.

Fickett, W. & Davis, W.C. 2000 *Detonation: Theory and Experiment*. Dover Publication.

Frederick, M.D., Gejji, R.M., Shepherd, J.E. & Slabaugh, C.D. 2023 Statistical analysis of detonation wave structure. *Proc. Combust. Inst.* **39** (3), 2847–2854.

Gamezo, V.N., Vasil'ev, A.A., Khokhlov, A.M. & Oran, E.S. 2000 Fine cellular structures produced by marginal detonations. *Proc. Combust. Inst.* **28** (1), 611–617.

Guo, H., Xu, Y., Zheng, H. & Zhang, H. 2023 Ignition limit and shock-to-detonation transition mode of n-heptane/air mixture in high-speed wedge flows. *Proc. Combust. Inst.* **39** (4), 4771–4780.

Gutiérrez Marcantoni, L.F., Tamagno, J. & Elaskar, S. 2017 Two-dimensional numerical simulations of detonation cellular structures in H_2-O_2-Ar mixtures with OpenFOAM®. *Intl J. Hydrogen Energ.* **42**, 26102–26113.

Han, W., Ma, W., Qian, C., Wen, J. & Wang, C. 2019 Bifurcation of pulsation instability in one-dimensional H_2-O_2 detonation with detailed reaction mechanism. *Phys. Rev. Fluids* **4**, 103202.

Huang, C., Wang, Y., Deiterding, R., Yu, D. & Chen, Z. 2022 Numerical studies on weak and strong ignition induced by reflected shock and boundary layer interaction. *Acta Mechanica Sin.* **38** (2), 121466.

Huang, Z., Lefebvre, M.H. & Van Tiggelen, P.J. 2000 Experiments on spinning detonations with detailed analysis of the shock structure. *Shock Waves* **10** (2), 119–125.

Ishii, K. & Grönig, H. 1998 Behavior of detonation waves at low pressures. *Shock Waves* **8** (1), 55–61.

Jasak, H. 1996 Error analysis and estimation for the finite volume method with applications to fluid flows. *PhD thesis*, Imperial College London, UK.

Jia, X., Xu, Y., Zheng, H. & Zhang, H. 2023 Direct detonation initiation in hydrogen/air mixture: effects of compositional gradient and hotspot condition. *J. Fluid Mech.* **970**, A22.

Kellenberger, M. & Ciccarelli, G. 2020 Single-head detonation propagation in a partially obstructed channel. *Combust. Flame* **215**, 283–294.

Kurganov, A., Noelle, S. & Petrova, G. 2001 Semi-discrete central-upwind scheme for hyperbolic conservation laws and Hamilton–Jacobi equations. *SIAM J. Sci. Comput.* **23** (3), 707–740.

Lau-Chapdelaine, S.S.M., Xiao, Q. & Radulescu, M.I. 2021 Viscous jetting and mach stem bifurcation in shock reflections: experiments and simulations. *J. Fluid Mech.* **908**, A18.

Lee, J.H.S. 2008 *The Detonation Phenomenon*. Cambridge University Press.

Lee, J.J., Garinis, D., Frost, D.L., Lee, J.H.S. & Knystautas, R. 1995 Two-dimensional autocorrelation function analysis of smoked foil patterns. *Shock Waves* **5** (3), 169–174.

Liang, Z. & Bauwens, L. 2005*a* Cell structure and stability of detonations with a pressure-dependent chain-branching reaction rate model. *Combust. Theor. Model.* **9** (1), 93–112.

LIANG, Z. & BAUWENS, L. 2005*b* Detonation structure with pressure-dependent chain-branching kinetics. *Proc. Combust. Inst.* **30** (2), 1879–1887.
LIANG, Z., BROWNE, S., DEITERDING, R. & SHEPHERD, J.E. 2007 Detonation front structure and the competition for radicals. *Proc. Combust. Inst.* **31** (2), 2445–2453.
LU, X., KAPLAN, C.R. & ORAN, E.S. 2021 A chemical-diffusive model for simulating detonative combustion with constrained detonation cell sizes. *Combust. Flame* **230**, 111417.
MACH, P. & RADULESCU, M.I. 2011 Mach reflection bifurcations as a mechanism of cell multiplication in gaseous detonations. *Proc. Combust. Inst.* **33** (2), 2279–2285.
MAHMOUDI, Y., KARIMI, N., DEITERDING, R. & EMAMI, S. 2014 Hydrodynamic instabilities in gaseous detonations: comparison of Euler, Navier–Stokes, and large-eddy simulation. *J. Propul. Power* **30** (2), 384–396.
MAHMOUDI, Y. & MAZAHERI, K. 2015 High resolution numerical simulation of triple point collision and origin of unburned gas pockets in turbulent detonations. *Acta Astronaut.* **115**, 40–51.
MAZAHERI, K., MAHMOUDI, Y. & RADULESCU, M.I. 2012 Diffusion and hydrodynamic instabilities in gaseous detonations. *Combust. Flame* **159**, 2138–2154.
MEAGHER, P.A., SHI, X., SANTOS, J.P., MURALEEDHARAN, N.K., CRANE, J., POLUDNENKO, A.Y., WANG, H. & ZHAO, X. 2023 Isolating gasdynamic and chemical effects on the detonation cellular structure: a combined experimental and computational study. *Proc. Combust. Inst.* **39** (3), 2865–2873.
MONNIER, V., RODRIGUEZ, V., VIDAL, P. & ZITOUN, R. 2022 An analysis of three-dimensional patterns of experimental detonation cells. *Combust. Flame* **245**, 112310.
NG, H.D., JU, Y. & LEE, J.H.S. 2007 Assessment of detonation hazards in high-pressure hydrogen storage from chemical sensitivity analysis. *Intl J. Hydrogen Energy* **32**, 93–99.
PENG, J., ZHANG, Z., HU, Z. & JIANG, Z. 2019 A theoretical and computational study of the vibration excitation on the transition criteria of shock wave reflections. *Aerosp. Sci. Technol.* **89**, 299–306.
PINTGEN, F., ECKETT, C.A., AUSTIN, J.M. & SHEPHERD, J.E. 2003 Direct observations of reaction zone structure in propagating detonations. *Combust. Flame* **133** (3), 211–229.
RADULESCU, M.I. 2018 A detonation paradox: why inviscid detonation simulations predict the incorrect trend for the role of instability in gaseous cellular detonations? *Combust. Flame* **195**, 151–162.
RADULESCU, M.I. & LEE, J.H.S. 2002 The failure mechanism of gaseous detonations: experiments in porous wall tubes. *Combust. Flame* **131** (1-2), 29–46.
RADULESCU, M.I., SHARPE, G.J., LAW, C.K. & LEE, J.H.S. 2007 The hydrodynamic structure of unstable cellular detonations. *J. Fluid Mech.* **580**, 31–81.
ROJAS CHAVEZ, S.B., CHATELAIN, K.P. & LACOSTE, D.A. 2023 Two-dimensional visualization of induction zone in hydrogen detonations. *Combust. Flame* **255**, 112905.
SEMENOV, A.N., BEREZKINA, M. & KRASSOVSKAYA, I.V. 2012 Classification of pseudo-steady shock wave reflection types. *Shock Waves* **22**, 307–316.
SHARPE, G.J. 2001 Transverse waves in numerical simulations of cellular detonations. *J. Fluid Mech.* **447**, 31–51.
SHARPE, G.J. & FALLE, S.A.E.G. 2000 Numerical simulations of pulsating detonations: I. Nonlinear stability of steady detonations. *Combust. Theor. Model.* **4**, 557–574.
SHI, X., ZHU, Y., YANG, J. & LUO, X. 2019 Mach stem deformation in pseudo-steady shock wave reflections. *J. Fluid Mech.* **861**, 407–421.
SOW, A., LAU-CHAPDELAINE, S.M. & RADULESCU, M.I. 2021 The effect of the polytropic index γ on the structure of gaseous detonations. *Proc. Combust. Inst.* **38**, 3633–3640.
STREHLOW, R.A., MAURER, R.E. & RAJAN, S. 1969 Transverse waves in detonations. I - Spacing in the hydrogen-oxygensystem. *AIAA J.* **7** (2), 323–328.
SUGIYAMA, Y. & MATSUO, A. 2012 Numerical investigation on the detonation regime with longitudinal pulsation in circular and square tubes. *Combust. Flame* **159** (12), 3646–3651.
SUGIYAMA, Y. & MATSUO, A. 2013 Numerical study of acoustic coupling in spinning detonation propagating in a circular tube. *Combust. Flame* **160** (11), 2457–2470.
TAYLOR, B.D., KESSLER, D.A., GAMEZO, V.N. & ORAN, E.S. 2013 Numerical simulations of hydrogen detonations with detailed chemical kinetics. *Proc. Combust. Inst.* **34** (2), 2009–2016.
TSUBOI, N. & HAYASHI, A.K. 2007 Numerical study on spinning detonations. *Proc. Combust. Inst.* **31** (2), 2389–2396.
TSUBOI, N., MORII, Y. & HAYASHI, A.K. 2013 Two-dimensional numerical simulation on galloping detonation in a narrow channel. *Proc. Combust. Inst.* **34** (2), 1999–2007.
TSUBOI, N., HAYASHI, A.K. & KOSHI, M. 2009 Energy release effect of mixture on single spinning detonation structure. *Proc. Combust. Inst.* **32** (2), 2405–2412.

WATANABE, H., MATSUO, A., CHINNAYYA, A., ITOUYAMA, N., KAWASAKI, A., MATSUOKA, K. & KASAHARA, J. 2023 Lagrangian dispersion and averaging behind a two-dimensional gaseous detonation front. *J. Fluid Mech.* **968**, A28.

XIAO, Q., SOW, A., MAXWELL, B.M. & RADULESCU, M.I. 2021 Effect of boundary layer losses on 2D detonation cellular structures. *Proc. Combust. Inst.* **38** (3), 3641–3649.

YAN, H., HAN, X., XIONG, H., SHI, C. & YOU, Y. 2024 Curved detonation and its reflections. *J. Fluid Mech.* **984**, A11.

YUAN, X., ZHOU, J., LIN, Z. & CAI, X. 2016 Adaptive simulations of detonation propagation in 90-degree bent tubes. *Intl J. Hydrogen Energy* **41** (40), 18259–18272.

ZADOK, N., ORUGANTI, S.K., ALVES, M.M. & KOZAK, Y. 2023 Dimensional analysis and simplified modeling for the cellular structure of premixed gas-phase detonation numerical simulations with single-step kinetics. *Combust. Flame* **256**, 112954.

ZHANG, B., LIU, H. & YAN, B. 2019 *a* Effect of acoustically absorbing wall tubes on the near-limit detonation propagation behaviors in a methane-oxygen mixture. *Fuel* **236**, 975–983.

ZHANG, Y., FANG, Y., NG, H.D. & TENG, H. 2019*b* Numerical investigation on the initiation of oblique detonation waves in stoichiometric acetylene–oxygen mixtures with high argon dilution. *Combust. Flame* **204**, 391–396.